

JPET Manuscript # 262287

Evolution of the Systems PK-PD Model for Antibody-drug Conjugates (ADC) to Characterize Tumor Heterogeneity and *In Vivo* Bystander Effect

Aman P. Singh, Gail M. Seigel, Leiming Guo, Ashwni Verma, Gloria Gao-Li Wong, Hsuan-Ping Cheng and Dhaval K. Shah

Department of Pharmaceutical Sciences, School of Pharmacy and Pharmaceutical Sciences, The State University of New York at Buffalo, Buffalo, NY (A.P.S., L.G., A.V., H.P.C., D.K.S.), Center for Hearing and Deafness, SUNY Eye Institute, The State University of New York at Buffalo, Buffalo, NY (G.M.S.) and Department of Biological Sciences, The State University of New York at Buffalo, Buffalo, NY (G.G.W.)

This work was supported by the Centre for Protein Therapeutics at University at Buffalo. D.K.S. is supported by NIH grant [GM114179] and [AI138195].

JPET Manuscript # 262287

Running Title: Systems PK-PD Model for ADC Bystander Effect

Corresponding authors:

Dhaval K. Shah, PhD

Department of Pharmaceutical Sciences

455 Pharmacy Building, School of Pharmacy and Pharmaceutical Sciences

University at Buffalo, The State University of New York

Buffalo, New York 14214-8033, USA

E-mail: dshah4@buffalo.edu

Aman P. Singh, PhD

(Past Address) Department of Pharmaceutical Sciences

455 Pharmacy Building, School of Pharmacy and Pharmaceutical Sciences

University at Buffalo, The State University of New York

Buffalo, New York 14214-8033, USA

E-mail: amanpree@buffalo.edu

(Current Address) Discovery and Translational Research, Biologics Development Sciences,
Janssen Biotherapeutics

1400 McKean Road

Spring House, Pennsylvania 19002, USA

E-mail: ASing215@its.jnj.com

Number of text pages: 47

Number of tables: 1

Number of figures: 8

Number of references: 28

Number of words:

Abstract: 245

Significance Statement: 79

Introduction: 778

Discussion: 1149

List of non-standard abbreviations: ADC – Antibody-drug conjugate; LC-MS – Liquid chromatography-Mass spectrometry; ELISA – Enzyme-linked immunosorbent assay; MMAE – Monomethyl Auristatin E; vc – valine-citrulline; T-vc-MMAE -Trastuzumab-vc-MMAE; DAR - Drug: Antibody Ratio; PK-PD - Pharmacokinetics Pharmacodynamics; TGI – Tumor Growth Inhibition

Recommended Section: Drug Metabolism, Transport, and Pharmacogenomics

JPET Manuscript # 262287

ABSTRACT

The objective of this work was to develop a systems PK-PD model that can characterize *in vivo* bystander effect of ADC in a heterogeneous tumor. To accomplish this goal a coculture xenograft tumor with 50% GFP-MCF7 (HER2-low) and 50% N87 (HER2-high) cells was developed. The relative composition of a heterogeneous tumor for each cell-type was experimentally determined by immunohistochemistry (IHC) analysis. Trastuzumab-vc-MMAE (T-vc-MMAE) was used as a tool ADC. Plasma and tumor PK of T-vc-MMAE was analyzed in N87, GFP-MCF7, and coculture tumor bearing mice. In addition, tumor growth inhibition (TGI) studies were conducted in all three xenografts at different T-vc-MMAE dose levels. To characterize the PK of ADC in coculture tumors, our previously published tumor distribution model was evolved to account for different cell populations. The evolved tumor PK model was able to *a priori* predict the PK of all ADC analytes in the coculture tumors reasonably well. The tumor PK model was subsequently integrated with a PD model that utilized intracellular tubulin occupancy to drive ADC efficacy in each cell-type. The final systems PK-PD model was able to simultaneously characterize all the TGI data reasonably well, with a common set of parameters for MMAE induced cytotoxicity. The model was later used to simulate the effect of different dosing regimen and tumor composition on the bystander effect of ADC. The model simulations suggested that dose-fractionation regimen may further improve overall efficacy and bystander effect of ADCs by prolonging the tubulin occupancy in each cell-type.

JPET Manuscript # 262287

SIGNIFICANCE

A PK-PD analysis is presented to understand bystander effect of Trastuzumab-vc-MMAE ADC in antigen (Ag)-low, Ag-high, and co-culture (i.e. Ag-high + Ag-low) xenograft mice. This study also describes a novel single cell-level systems PK-PD model to characterize *in vivo* bystander effect of ADCs. The proposed model can serve as a platform to mathematically characterize multiple cell populations and their interactions in tumor tissues. Our analysis also suggests that fractionated dosing regimen may help improve the bystander effect of ADCs.

JPET Manuscript # 262287

INTRODUCTION

Antibody-drug conjugates (ADCs) are novel anticancer drug molecules (Lambert, 2015; Mantaj et al., 2017), which are designed to expand the therapeutic window of chemotherapeutic agents by targeting them to antigen expressing tumor cells via monoclonal antibodies (mAbs). At present there are five FDA approved ADCs and >80 molecules in the clinical development (Anthony L, 2018). While these molecules are promising, their efficacy is often limited by poor tumor distribution (Cilliers et al., 2016) and heterogeneity in antigen expressing (Ag⁺) cells (Seol et al., 2012). These limitations can be overcome with the help of ‘bystander effect’, which promotes more homogenous distribution of payload within a solid tumor (Kovtun et al., 2006; Singh et al., 2016b). Once the ADC molecules bind to Ag⁺ cells in a heterogeneous tumor, they get internalized and release the payload, a fraction of which kills the Ag⁺ cells and the rest diffuse out and kill the bystander antigen negative (Ag⁻) cells, leading to a phenomenon known as the bystander effect (Singh et al., 2016b). While this phenomenon is qualitatively confirmed using *in vitro* and *in vivo* investigations (Kovtun et al., 2006; Ogitani et al., 2016), the rate and extent of bystander effect within a heterogeneous tumor is not quantitatively determined or mathematically characterized to date. To further enhance quantitative understanding of this phenomenon, here we present an *in vivo* investigation and development of a systems pharmacokinetic-pharmacodynamic (PK-PD) model to characterize *in vivo* bystander effect of ADCs. Development of such models can be crucial for identifying drug- and system-specific parameters that are important for accomplishing *in vivo* bystander effect (Singh et al., 2015a; Singh et al., 2015b; Singh and Shah, 2017a; Singh and Shah, 2018). In addition, these models could also be used to guide the development of next-generation ADCs (van Geel et al., 2015), evaluate druggability of novel targets, and facilitate preclinical-to-clinical translation of ADC efficacy.

JPET Manuscript # 262287

In the past we have presented quantitative investigation to understand *in vitro* bystander effect of ADCs using anti-HER2 ADC Trastuzumab-vc-MMAE (T-vc-MMAE) as a tool compound. Upon internalization this ADC can release the lipophilic payload MMAE in its pure form, which is capable of partitioning into the nearby cells and exhibit bystander killing. Using *in vitro* cocultures of HER2-high N87 (Ag+) and HER2-low GFP-MCF7 (Ag-) cells, we have investigated rate and extent of ADC induced bystander effect, and evaluated how the presence of different percentage of Ag+ cells affect the bystander killing of Ag- cells (Singh et al., 2016b). During these investigations we observed that there was a notable delay between ADC exposure and the occurrence of bystander effect, which may have stemmed from the time taken by the cells to process the ADCs. Consequently, we further investigated cellular processing of T-vc-MMAE using *in vitro* PK studies. With the help of the PK data we were able to develop a unique single-cell PK model for ADCs, which was able to integrate key drug- and system-specific parameters in a mathematical format to characterize ADC processing within different cell lines (Singh and Shah, 2017b). We further expanded this single-cell PK model to develop an *in vitro* systems PK-PD model, which employed intracellular occupancy of the pharmacological target (i.e. tubulin) by MMAE to drive direct- and bystander-killing of cancer cells by the ADC (Singh and Shah, 2019). This unique single-cell PK-PD model has also been translated to *in vivo* scenarios recently, to characterize tumor PK of T-vc-MMAE, and tumor growth inhibition (TGI) by T-vc-MMAE in GFP-MCF7 and N87 xenografts (Singh et al., 2019).

Here we have expanded the application of cell-level PK-PD model towards characterizing *in vivo* bystander effect for T-vc-MMAE in a heterogeneous tumor model developed using GFP-MCF7 and N87 cells. Both the cell lines were inoculated in a mouse to develop a 50:50 coculture xenograft tumor model. PK and PD (i.e. TGI) of T-vc-MMAE was investigated in the coculture

JPET Manuscript # 262287

xenograft. In order to quantitatively characterize tumor PK of ADC, our previously published tumor disposition model was evolved to account for tumor heterogeneity. The model also accounted for interaction of T-vc-MMAE and released MMAE with two different cell populations in the tumor, and distinct growth characteristics of each cell population. The evolved model was able to *a priori* predict tumor PK of T-vc-MMAE in the heterogeneous tumor model. Subsequently, the tumor PK model was integrated with our previously published single-cell PK-PD model to characterize T-vc-MMAE induced direct and bystander killing of cancer cells in the coculture tumor. The final systems PK-PD model was used to evaluate the effect of different dosing regimen and tumor composition on the bystander effect of ADC. The presented PK-PD model could be translated to predict the bystander effect of ADCs in the clinic using the strategies presented by us before (Shah et al., 2012; Singh and Shah, 2017a).

JPET Manuscript # 262287

MATERIALS AND METHODS

Cell lines:

HER2-expressing cell lines NCI-N87 and green fluorescent protein transfected (GFP) MCF7 were cultured using their recommended media conditions (Singh et al., 2016b; Singh and Shah, 2017b). HER2 expression level in N87 and GFP-MCF7 cells has been reported to be ~950,000 and ~55,000 receptors per cell, which makes them HER2-high and HER2-low cell lines, respectively (Singh and Shah, 2017b). Expression of GFP in MCF7 cells enables their detection within *in vitro* and *in vivo* coculture system (Singh et al., 2016b).

Tool ADC:

The tool ADC Trastuzumab-vc-MMAE was synthesized and characterized in-house. Commercially available Trastuzumab (Herceptin®, Genentech) was conjugated with valine-citrulline MMAE (drug-linker solution) using random conjugation method, resulting in a heterogeneous formulation with an average drug: antibody ratio (DAR) of ~4. Detailed protocols on synthesis and characterization of T-vc-MMAE have been published before (Singh et al., 2016b; Singh and Shah, 2017b).

Development of N87 and GFP-MCF7 monoculture xenografts:

Six weeks old male severe combined immunodeficient (NOD.CB17-*Prkdc*^{scid}/J) mice were purchased from Jackson Laboratory (USA). After acclimation, mice were subcutaneously implanted with ~10 million tumor cells (N87 or GFP-MCF7) suspended in their growth medium. To facilitate faster growth of GFP-MCF7 bearing tumors, mice were supplemented with 1μg of 17β-estradiol valerate (Sigma®) in 50μL of pharmaceutical grade peanut oil (Sigma®) via subcutaneous injection every 4 days (Donoghue et al., 2012). All procedures were approved by

JPET Manuscript # 262287

the Institutional Animal Care and Use Committee (IACUC) at State University of New York at Buffalo.

Development of N87 and GFP-MCF7 coculture xenografts:

Due to variable growth patterns of N87 and GFP-MCF7 cells, different ratios of two cell-types were initially implanted to find out a ratio that would yield 50:50 coculture xenograft at the time of ADC administration. After optimization, a mixture of ~ 1 million GFP-MCF7 and ~9 million N87 cells suspended in a similar ratio (1:9) of their cell culture medium was used to achieve 50:50 coculture at tumor volumes ~350-400 mm³. To enable successful growth of GFP-MCF7 cells, and to maintain consistency, mice were also supplemented with subcutaneous dosing of 17 β -estradiol valerate as mentioned before.

Immunohistochemical (IHC) analysis of heterogeneous tumors:

Heterogeneous tumors were grown in SCID mice by inoculating ~1 million GFP-MCF7 and ~9 million N87 cells, as described earlier. Once the tumors reached a volume of 350-400 mm³, mice were sacrificed, and tumors were surgically removed. The harvested tissues were fixed in 4% paraformaldehyde for 24 hours and were later transferred to 70% ethanol. The tissues were then embedded in paraffin and 4 (μ m) micron thick sections were cut using a microtome from an upper, middle and lower part of a spherical tumor. The obtained sections were rinsed in phosphate buffer saline (PBS, PH 7.4) twice, and later stained using DAPI (Sigma®) at a working concentration of 1 μ g/mL for 5 mins at room temperature in the dark. The stained slides were imaged using Zeiss AxioImager upright microscope to measure the fluorescence emitted from GFP label (excitation: 488 nm: emission: 510 nm) and DAPI (excitation: 360 nm: emission: 460 nm) counterstain. To perform semi-quantitative analysis of IHC images the images obtained from the middle sections

JPET Manuscript # 262287

of coculture tumors (n=3) were analyzed using ImageJ software (Schneider et al., 2012). Percentage of areas emitting fluorescence from GFP label and DAPI counterstain were calculated. Since DAPI will stain the nuclei of all tumor cells, the percentage of a given section emitting blue fluorescence from DAPI will reflect the fraction of tumor area covered with both cell-type (i.e. N87 or GFP-MCF7). Whereas, the percentage of given section emitting green fluorescence from GFP will reflect the fraction of tumor area covered with only GFP-MCF7 cells. The ratio of these two measurements should provide a rough estimate of the fraction of each cell-type within a heterogeneous tumor.

Bioanalytical techniques to measure plasma and tumor concentrations of ADC:

Three different analytical methods were developed to measure plasma and tumor PK of T-vc-MMAE. An ELISA method was utilized to measure total Trastuzumab concentrations, whereas an LC-MS/MS method was used to measure free MMAE concentrations in plasma and tumor homogenate samples. A forced deconjugation method using papain enzyme was employed to deconjugate the antibody-conjugated MMAE in a biological sample, which enabled the measurement of total MMAE in plasma and tumor samples. Detailed methodology for the development and validation of these analytical techniques (Singh and Shah, 2017b), and their application for *in vitro* and *in vivo* experiments (Singh et al., 2019), have been published before.

Plasma and tumor pharmacokinetic studies:

Total 30 SCID mice were equally divided into 3 groups, which were then inoculated with GFP-MCF7 (Group A, n=10), N87 cells (Group B, n=10), or 1:9 mixture of GFP-MCF7 and N87 cells (Group C, n=10). Treatment was initiated 3 to 6 weeks after implantation, when the tumors were ~400 mm³. Nine out of ten animals from each group (A, B or C) were treated with a single dose

JPET Manuscript # 262287

of 10 mg/kg T-vc-MMAE intravenously, whereas one untreated animal from each group was sacrificed to harvest blood and tumor samples on Day 0. Treated animals were further divided into three different subgroups (n=3) corresponding to 24h (A1, B1, C1), 72h (A2, B2, C2), and 168h (A3, B3, C3) time points. At each time point blood samples were collected via cardiac puncture and tumor tissues were surgically removed. In addition, a blood sample was collected from one animal in each subgroup (n=3) at 10 mins. Harvested blood samples were immediately processed to separate plasma, and all plasma and tumor samples were stored at -80°C until further analysis.

Tumor growth inhibition studies:

Single dose therapy of HER2-high N87 xenografts with T-vc-MMAE:

Total 28 SCID mice were subcutaneously inoculated with N87 cells, and the treatment was initiated 4-6 weeks after tumor implantation when the tumor volumes reached ~400 mm³. At day 0, mice were randomly assigned to 4 equal groups: control (no treatment, n=7), 1 mg/kg T-vc-MMAE (n=7), 3 mg/kg T-vc-MMAE (n=7), and 10 mg/kg T-vc-MMAE.

Single dose therapy of HER2-low GFP-MCF7 xenografts with T-vc-MMAE:

Total 25 SCID mice were subcutaneously inoculated with GFP-MCF7 cells, and the treatment was initiated 3-5 weeks after tumor implantation when the tumor volumes reached ~400 mm³. At day 0, mice were randomly assigned to 4 different groups: control (no treatment, n=6), 3 mg/kg T-vc-MMAE (n=7), 5 mg/kg T-vc-MMAE (n=5), and 10 mg/kg T-vc-MMAE (n=7).

Single dose therapy of 50:50 coculture xenografts of N87 and GFP-MCF7 cells with T-vc-MMAE:

Total 20 SCID mice were subcutaneously inoculated with a mixture of GFP-MCF7 and N87 cells (ratio 1:9), and the treatment was initiated 3-5 weeks after tumor implantation when the tumor

JPET Manuscript # 262287

volumes reached $\sim 400 \text{ mm}^3$. At day 0, mice were randomly assigned to 4 equal groups: control (no treatment, $n=5$), 3 mg/kg T-vc-MMAE ($n=5$), 5 mg/kg T-vc-MMAE ($n=5$), and 10 mg/kg T-vc-MMAE ($n=5$).

Tumor volumes were calculated by measuring length (L, distance between longest diameter) and breadth (B) of tumors using vernier caliper and using the following formula: $\frac{1}{2} \times L \times B^2$. Tumor volumes were measured twice a week, until the tumor volume exceeded $>2500 \text{ mm}^3$ cutoff or the tumor was completely regressed for a prolonged duration of time (~ 3 weeks).

Development of the systems PK-PD model to characterize *in vivo* bystander effect of Trastuzumab-vc-MMAE:

Plasma pharmacokinetic model for T-vc-MMAE:

A previously established plasma PK model for ADCs (shown as a part of Figure-3) was used to build this model. Since plasma PK of ADC was similar between N87, GFP-MCF7, and coculture xenografts, plasma PK data from all three mouse models were pooled to estimate the model parameters. Briefly, the biexponential PK profile of ADC is characterized using a 2-compartment model with linear catabolic clearance (CL_{ADC}) from the central compartment. The distribution of ADC to peripheral tissues is characterized using a distributional clearance parameter (CLD_{ADC}). An additional 1st order elimination rate constant coined as ‘non-specific deconjugation rate’ (K_{dec}^P) is incorporated in the central compartment, to characterize non-specific deconjugation of MMAE from the ADC. This rate also contributes towards the 1st order decline in average DAR value of the ADC. Both elimination pathways (CL_{ADC} and K_{dec}^P) generate free (unconjugated) MMAE, and hence become the formation rates for MMAE. The disposition of free MMAE is also characterized using a 2-compartment model with linear systemic clearance (CL_{Drug}) and distributional clearance

JPET Manuscript # 262287

(CLD_{Drug}) (Shah et al., 2012; Shah et al., 2014; Khot et al., 2015; Singh et al., 2015b; Singh et al., 2016a; Singh and Shah, 2017a; Singh and Shah, 2018).

Tumor distribution model for T-vc-MMAE:

Distribution of T-vc-MMAE and released MMAE in solid tumors was characterized using the tumor disposition model shown in Figure-3. Two distinct exchange processes (i.e. surface and vascular exchange) are incorporated to describe the mechanistic distribution of T-vc-MMAE and free MMAE from systemic circulation to tumor extracellular space. Due to high interstitial pressure and lack of functional lymphatic system within the tumor microenvironment, it is assumed that the disposition of ADC and released drug is limited to diffusive processes, with a lack of any convective transport. Within the original work published by Wittrup et al. (Thurber et al., 2008a; Thurber et al., 2008b), molecular size-specific diffusivity and permeability parameters have been reported. Additionally, with an assumption of a spherical tumor, size/radius of the tumor was used to determine the rate of ADC/released drug exchange via surface and vascular processes. At lower tumor volumes surface exchange predominates, and at higher tumor volumes vascular exchange is more predominant (Thurber et al., 2008a; Thurber et al., 2008b). With changing tumor volumes due to ADC efficacy, the relative significance of these pathways also varies.

Incorporation of single cell pharmacokinetic model to account for ADC processing by N87 and GFP-MCF7 cells:

Once in the tumor extracellular space, the disposition of T-vc-MMAE and released MMAE within each cell-type (N87 or GFP-MCF7) was characterized using a single-cell disposition model (Figure-3) (Singh and Shah, 2017b). It was assumed that there are $\sim 10^8$ tumor cells per gram of tumor (Monte, 2009). Exchange of T-vc-MMAE and free MMAE between each cell-type and

JPET Manuscript # 262287

extracellular space was characterized simultaneously. Key processes in the model include T-vc-MMAE binding (K_{on}^{ADC} and K_{off}^{ADC}) to HER2 receptors on the tumor cells, and internalization (K_{int}^{ADC}) and intracellular degradation (K_{deg}^{ADC}) of ADC in the endosomal/lysosomal space, which leads to the release of the free (unconjugated) MMAE in the cytoplasm. The released MMAE within the cytoplasmic space is assumed to either bind to intracellular tubulin (K_{on}^{Tub} and K_{off}^{Tub}) or exchange with the extracellular space using influx (K_{in}^{Drug}) and efflux (K_{out}^{Drug}) processes. Once the free MMAE is released in the tumor extracellular space, it can either distributes to other cancer cells or diffuse out into the systemic circulation.

To conserve mass-balance within the dynamic system of two distinctly growing tumor cell populations, a dilution factor was incorporated within the single cell PK model for each cell-type. This dilution factor renders dilution of intracellular content (either intact ADC or released drug) at the rate equivalent to the growth rate (K_g^{Tumor}) of each cell-type.

Equations pertaining to the growth of each cell type (i.e. N87 or GFP-MCF7) within the heterogeneous tumor (Tumor volume (TV), in L) are provided below. 50:50 coculture composition was used as the initial condition.

$$\frac{d(TV_{mm3}^{N87})}{dt} = \frac{\ln 2}{DT^{N87}} \cdot TV_{mm3}^{N87} \quad \text{Initial Condition (IC)} = \frac{1}{2} \cdot TV_{mm3}^0 \quad (1)$$

$$\frac{d(TV_{mm3}^{MCF7})}{dt} = \frac{\ln 2}{DT^{MCF7}} \cdot TV_{mm3}^{MCF7} \quad IC = \frac{1}{2} \cdot TV_{mm3}^0 \quad (2)$$

$$TV_{mm3} = TV_{mm3}^{N87} + TV_{mm3}^{MCF7} \quad (3)$$

$$TV_{mm3} = TV \cdot 10^6 \quad R_{Tumor} = \left[\frac{3 \cdot TV \cdot 1000}{4\pi} \right]^{1/3} \quad (4)$$

Above, TV_{mm3}^0 , corresponds to initial tumor volume of the heterogenous tumor at the beginning of the treatment.

JPET Manuscript # 262287

Equations associated with plasma pharmacokinetics and tumor distribution of T-vc-MMAE (in amounts) and unconjugated MMAE (in concentrations) are provided below.

$$\begin{aligned} \frac{d(X1_{ADC})}{dt} = & -\frac{CL_{ADC}}{V1_{ADC}} \cdot X1_{ADC} - \frac{CLD_{ADC}}{V1_{ADC}} \cdot X1_{ADC} + \frac{CLD_{ADC}}{V2_{ADC}} \cdot X2_{ADC} - K_{dec}^P \\ & \cdot X1_{ADC} - \left(\frac{X1_{ADC}}{V1_{ADC}} - \frac{ADC_f^{ex}}{\epsilon^{ADC}} \right) \cdot TV \cdot \left(\frac{2 \cdot P_{ADC} \cdot R_{Cap}}{R_{Krogh}^2} + \frac{6 \cdot D_{ADC}}{R_{Tumor}^2} \right) \end{aligned} \quad (5)$$

$$\frac{d(X2_{ADC})}{dt} = \frac{CLD_{ADC}}{V1_{ADC}} \cdot X1_{ADC} - \frac{CLD_{ADC}}{V2_{ADC}} \cdot X2_{ADC} \quad (6)$$

$$\begin{aligned} \frac{d(C1_{Drug})}{dt} = & -\frac{CL_{Drug}}{V1_{Drug}} \cdot C1_{Drug} - \frac{CLD_{Drug}}{V1_{Drug}} \cdot C1_{Drug} + \frac{CLD_{Drug}}{V1_{Drug}} \cdot C2_{Drug} \\ & + \frac{(K_{dec}^P \cdot X1_{ADC} \cdot \overline{DAR})}{V1_{Drug}} + \frac{CL_{ADC} \cdot \overline{DAR} \cdot \frac{X1_{ADC}}{V1_{ADC}}}{V1_{Drug}} \\ & - \left(C1_{Drug} - \frac{Drug_f^{ex}}{(TV \cdot \epsilon^{Drug})} \right) \cdot \left(\frac{2 \cdot P_{Drug} \cdot R_{Cap}}{R_{Krogh}^2} + \frac{6 \cdot D_{Drug}}{R_{Tumor}^2} \right) \end{aligned} \quad (7)$$

$$\frac{d(C2_{Drug})}{dt} = \frac{CLD_{Drug}}{V2_{Drug}} \cdot C1_{Drug} - \frac{CLD_{Drug}}{V2_{Drug}} \cdot C2_{Drug} \quad (8)$$

$$\frac{d(\overline{DAR})}{dt} = -K_{dec}^P \cdot \overline{DAR} \quad (9)$$

Above, initial conditions for equations 5 and 9 are Dose^{ADC} (injected intravenous dose of ADC) and $\overline{DAR}(0)$ (initial average DAR of drug formulation), respectively. Initial conditions for the rest of the equations are zero. Equations associated with the concentration of T-vc-MMAE and amounts of unconjugated MMAE in tumor extracellular space are listed below:

JPET Manuscript # 262287

$$\begin{aligned} \frac{d(ADC_f^{ex})}{dt} = & \left(\frac{X1_{ADC}}{V1_{ADC}} - \frac{ADC_f^{ex}}{\epsilon_{ADC}} \right) \cdot \left(\frac{2 \cdot P_{ADC} \cdot R_{Cap}}{R_{Krogh}^2} + \frac{6 \cdot D_{ADC}}{R_{Tumor}^2} \right) \\ & + \left(-K_{on}^{ADC} \cdot \frac{ADC_f^{ex}}{\epsilon_{ADC}} \cdot (Ag_{Ex}^{N87} - ADC_b^{N87}) + K_{off}^{ADC} \cdot ADC_b^{N87} \right) \\ & \cdot \frac{NC^{N87} \cdot SF}{TV} \\ & + \left(-K_{on}^{ADC} \cdot \frac{ADC_f^{ex}}{\epsilon_{ADC}} \cdot (Ag_{Ex}^{MCF7} - ADC_b^{MCF7}) + K_{off}^{ADC} \cdot ADC_b^{MCF7} \right) \\ & \cdot \frac{NC^{MCF7} \cdot SF}{TV} - K_{dec}^p \cdot ADC_f^{ex} \end{aligned} \quad (10)$$

$$\begin{aligned} \frac{d(Drug_f^{ex})}{dt} = & \left(C1_{Drug} - \frac{Drug_f^{ex}}{(TV \cdot \epsilon_{Drug})} \right) \cdot TV \\ & \cdot \left(\frac{2 \cdot P_{Drug} \cdot R_{Cap}}{R_{Krogh}^2} + \frac{6 \cdot D_{Drug}}{R_{Tumor}^2} \right) + K_{dec}^p \cdot ADC_f^{ex} \cdot \overline{DAR} \cdot TV \\ & + (K_{dec}^p \cdot ADC_b^{N87} \cdot \overline{DAR} + K_{out}^{Drug} \cdot Drug_f^{N87}) \cdot NC^{N87} \cdot SF \\ & + (K_{dec}^p \cdot ADC_b^{MCF7} \cdot \overline{DAR} + K_{out}^{Drug} \cdot Drug_f^{MCF7}) \cdot NC^{MCF7} \\ & \cdot SF - K_{in}^{Drug} \cdot NC^{N87} \cdot \left(\frac{V^{N87}}{TV \cdot \epsilon_{Drug}} \right) \cdot Drug_f^{ex} - K_{in}^{Drug} \\ & \cdot NC^{MCF7} \cdot \left(\frac{V^{MCF7}}{TV \cdot \epsilon_{Drug}} \right) \cdot Drug_f^{ex} \end{aligned} \quad (11)$$

Equations associated with cellular disposition of T-vc-MMAE and unconjugated MMAE in each cell-type '*i*' (where '*i*' can be either N87 or GFP-MCF7 cell) are provided below. Concentrations are represented in the form of number of molecules of each analyte per single tumor cell.

$$\begin{aligned} \frac{d(ADC_b^i)}{dt} = & K_{on}^{ADC} \cdot \frac{ADC_f^{ex}}{\epsilon_{ADC}} \cdot (Ag_{Ex}^i - ADC_b^i) - K_{off}^{ADC} \cdot ADC_b^i - (K_{dec}^p + K_{int}^{ADC}) \cdot ADC_b^i \\ & - \frac{\ln 2}{DT^i} \cdot ADC_b^i \end{aligned} \quad (12)$$

JPET Manuscript # 262287

$$\frac{d(\text{ADC}_{\text{lyso}}^i)}{dt} = K_{\text{int}}^{\text{ADC}} \cdot \text{ADC}_{\text{b}}^i - K_{\text{deg}}^{\text{ADC}} \cdot \text{ADC}_{\text{lyso}}^i - \frac{\text{Ln } 2}{\text{DT}^i} \cdot \text{ADC}_{\text{lyso}}^i \quad (13)$$

$$\begin{aligned} \frac{d(\text{Drug}_{\text{f}}^i)}{dt} = & K_{\text{deg}}^{\text{ADC}} \cdot \text{ADC}_{\text{lyso}}^i \cdot \overline{\text{DAR}} - K_{\text{out}}^{\text{Drug}} \cdot \text{Drug}_{\text{f}}^i - K_{\text{on}}^{\text{Tub}} \cdot \text{Drug}_{\text{f}}^i \\ & \cdot (\text{Tub}_{\text{tot}}^i - \text{Drug}_{\text{b}}^i) + K_{\text{off}}^{\text{Tub}} \cdot \text{Drug}_{\text{b}}^i + K_{\text{in}}^{\text{Drug}} \cdot \left(\frac{V^i}{\text{TV} \cdot \varepsilon^{\text{Drug}}} \right) \cdot \left(\frac{\text{Drug}_{\text{f}}^{\text{ex}}}{\text{SF}} \right) \\ & - \frac{\text{Ln } 2}{\text{DT}^i} \cdot \text{Drug}_{\text{f}}^i \end{aligned} \quad (14)$$

$$\frac{d(\text{Drug}_{\text{b}}^i)}{dt} = K_{\text{on}}^{\text{Tub}} \cdot \text{Drug}_{\text{f}}^i \cdot (\text{Tub}_{\text{tot}}^i - \text{Drug}_{\text{b}}^i) - K_{\text{off}}^{\text{Tub}} \cdot \text{Drug}_{\text{b}}^i - \frac{\text{Ln } 2}{\text{DT}^i} \cdot \text{Drug}_{\text{b}}^i \quad (15)$$

Above, the initial conditions for equations 10-15 are zero.

Calculation of intracellular tubulin occupancy in each cell-type:

Upon integration of tumor distribution model with single cell PK model, the percent occupancy of tubulin by MMAE inside each tumor cell can be calculated by dividing the number of tubulin-bound MMAE molecules with the number of total tubulin molecules inside each cell-type 'i' (where 'i' can be either N87 or GFP-MCF7 cell). The relevant equation is provided below:

$$\text{Occ}_{\text{tub}}^i = \left(\frac{\text{Drug}_{\text{b}}^i}{\text{Tub}_{\text{tot}}^i} \right) \cdot 100 \quad (16)$$

Driving direct killing and bystander effect of ADC using intracellular tubulin occupancy:

TGI data generated using different dose levels of ADC in all three mouse models (i.e. N87, GFP-MCF7, and coculture) were used to develop a systems PK-PD model that could account for direct killing and bystander effect of ADCs *in vivo* (Figure 5). First, the coculture tumor PK model was used to predict intracellular occupancy of tubulin in each cell-type. The intracellular occupancy

JPET Manuscript # 262287

was then used to drive the cytotoxicity of each cell-type, using a non-linear killing function that shuttles the growing tumor cells into non-growing phases, which eventually die. This model is also known as the ‘cell-distribution model’ (Yang et al., 2010). It was assumed that among all different cell populations (growing or non-growing) the processing of ADC was active, and upon the death of each cell-type the intracellular content (either intact T-vc-MMAE or free MMAE) comes out and becomes the part of extracellular space. The released intracellular content could then re-distribute back into other cells or diffuse out into the systemic circulation via surface or vascular exchange processes (Figure 5). The resulting equations characterizing tumor growth dynamics of each cell-type ‘ i ’ (where ‘ i ’ can be either N87 or GFP-MCF7 cell) are provided below:

Growth rate:

$$Kg^i = \left(\frac{\text{Ln } 2}{DT^i} \right) \quad (17)$$

Killing rate:

$$\text{Kill}^i = \left\{ \frac{K_{\max} \cdot (\text{Occ}_{\text{tub}}^i)^{\gamma}}{(KC50)^{\gamma} + (\text{Occ}_{\text{tub}}^i)^{\gamma}} \right\} \quad (18)$$

$$\frac{d(TV_i^1)}{dt} = (Kg^i - \text{Kill}^i) \cdot TV_i^1 \quad (19)$$

$$\frac{d(TV_i^2)}{dt} = \text{Kill}^i \cdot TV_i^1 - \frac{1}{\tau} \cdot TV_i^2 \quad (20)$$

$$\frac{d(TV_i^3)}{dt} = \frac{1}{\tau} \cdot (TV_i^2 - TV_i^3) \quad (21)$$

$$\frac{d(TV_i^4)}{dt} = \frac{1}{\tau} \cdot (TV_i^3 - TV_i^4) \quad (22)$$

$$TV_{\text{mm}3}^i = TV_i^1 + TV_i^2 + TV_i^3 + TV_i^4 \quad (23)$$

$$TV_{\text{mm}3} = TV_{\text{mm}3}^{\text{N87}} + TV_{\text{mm}3}^{\text{MCF7}} \quad (24)$$

JPET Manuscript # 262287

The equations for concentration of T-vc-MMAE (eq.10) and amount of MMAE (eq.11) in the tumor extracellular space were updated to have inputs from intracellular content of the last transit compartment (TV_i^4) for each cell-type (N87 or GFP-MCF7). The resulting equations are provided below:

$$\begin{aligned} \frac{d(ADC_f^{ex})}{dt} = & \left(\frac{X1_{ADC}}{V1_{ADC}} - \frac{ADC_f^{ex}}{\epsilon_{ADC}} \right) \cdot \left(\frac{2 \cdot P_{ADC} \cdot R_{Cap}}{R_{Krogh}^2} + \frac{6 \cdot D_{ADC}}{R_{Tumor}^2} \right) \\ & + \left(-K_{on}^{ADC} \cdot \frac{ADC_f^{ex}}{\epsilon_{ADC}} \cdot (Ag_{Ex}^{N87} - ADC_b^{N87}) + K_{off}^{ADC} \cdot ADC_b^{N87} \right) \cdot \frac{NC^{N87} \cdot SF}{TV} \\ & + \left(-K_{on}^{ADC} \cdot \frac{ADC_f^{ex}}{\epsilon_{ADC}} \cdot (Ag_{Ex}^{MCF7} - ADC_b^{MCF7}) + K_{off}^{ADC} \cdot ADC_b^{MCF7} \right) \\ & \cdot \frac{NC^{MCF7} \cdot SF}{TV} - K_{dec}^p \cdot ADC_f^{ex} + \frac{1}{\tau} \cdot TV_{N87}^4 \cdot 10^5 \cdot (ADC_b^{N87} + ADC_{lyso}^{N87}) \\ & \cdot \frac{SF}{TV} + \frac{1}{\tau} \cdot TV_{MCF7}^4 \cdot 10^5 \cdot (ADC_b^{MCF7} + ADC_{lyso}^{MCF7}) \cdot \frac{SF}{TV} \end{aligned} \quad (25)$$

$$\begin{aligned} \frac{d(Drug_f^{ex})}{dt} = & \left(C1_{Drug} - \frac{Drug_f^{ex}}{(TV \cdot \epsilon_{Drug})} \right) \cdot TV \cdot \left(\frac{2 \cdot P_{Drug} \cdot R_{Cap}}{R_{Krogh}^2} + \frac{6 \cdot D_{Drug}}{R_{Tumor}^2} \right) + K_{dec}^p \\ & \cdot ADC_f^{ex} \cdot \overline{DAR} \cdot TV + (K_{dec}^p \cdot ADC_b^{N87} \cdot \overline{DAR} + K_{out}^{Drug} \cdot Drug_f^{N87}) \cdot NC^{N87} \\ & \cdot SF + (K_{dec}^p \cdot ADC_b^{MCF7} \cdot \overline{DAR} + K_{out}^{Drug} \cdot Drug_f^{MCF7}) \cdot NC^{MCF7} \cdot SF \\ & - K_{in}^{Drug} \cdot NC^{N87} \cdot \left(\frac{V^{N87}}{TV \cdot \epsilon_{Drug}} \right) \cdot Drug_f^{ex} - K_{in}^{Drug} \cdot NC^{MCF7} \cdot \left(\frac{V^{MCF7}}{TV \cdot \epsilon_{Drug}} \right) \\ & \cdot Drug_f^{ex} + \frac{1}{\tau} \cdot TV_{N87}^4 \cdot 10^5 \cdot (Drug_f^{N87} + Drug_b^{N87}) \cdot SF + \frac{1}{\tau} \cdot TV_{MCF7}^4 \\ & \cdot 10^5 \cdot (Drug_f^{MCF7} + Drug_b^{MCF7}) \cdot SF \end{aligned} \quad (26)$$

Parameter Estimation, Model Fitting, and Simulations:

A priori prediction of tumor pharmacokinetics of T-vc-MMAE in the coculture tumor model:

JPET Manuscript # 262287

Our previously developed tumor PK model for N87 and GFP-MCF7 xenografts (Singh et al., 2019) was evolved to account for heterogeneous tumor cell population (Figure-3). Two distinct populations of tumor cell-types was assumed, and previously published parameters (Table 1) were utilized to *a priori* predict tumor exposure of different ADC analytes (i.e. free MMAE, total MMAE, and total Trastuzumab). The PK was predicted following intravenous administration of 10 mg/kg T-vc-MMAE in a mouse bearing 50:50 coculture tumor.

Simulations of free and total MMAE exposures at different dose-levels in three mouse models:

After validation of the tumor PK model for the heterogeneous tumor, simulations were performed to predict free and total MMAE exposures in the heterogeneous tumor after intravenous dose of 0.1, 1, and 10 mg/kg dose. The predicted PK profiles in 50:50 coculture tumor were compared with the PK profiles in N87 and GFP-MCF7 monoculture tumors.

Simulations for intracellular tubulin occupancy within each cell-type in a heterogenous tumor:

Simulations for percent tubulin occupancy in each cell-type (i.e. N87 and GFP-MCF7) of 50:50 coculture tumor were performed at 0.1-10 mg/kg doses of T-vc-MMAE. In addition, an improvement in the percentage tubulin occupancy of GFP-MCF7 (HER2-low) cell with increasing fractions of N87 (HER2-high) cells in a heterogeneous tumor was also simulated at 0.1-10 mg/kg doses. The improvement in percentage tubulin occupancy of Ag- cells is used as a driver for ADC bystander effect.

Simultaneous fittings of TGI datasets from N87, GFP-MCF, and 50:50 Coculture xenografts:

Step 1: Individual tumor growth profiles of N87 and GFP-MCF7 xenografts from the control group were fitted to an exponential growth model (eq. 17). Due to the observed variability in the individual tumor growth profiles, a mean tumor doubling time (DT^{N87} , DT^{MCF7}) and inter-subject

JPET Manuscript # 262287

variability with log-normal distribution ($IIV^{DT^{N87}}$, $IIV^{DT^{MCF7}}$) were estimated for each xenograft (N87 and GFP-MCF7). To characterize the tumor growth of the coculture xenografts, it was assumed that at time 0 the composition of the heterogeneous tumor included 50:50 ratio of both the cell-types. The estimated mean doubling times associated with N87 and GFP-MCF7 tumors were fixed to previously obtained values, and the individual tumor growth profiles in the control group for all three mouse models (N87, GFP-MCF7 and coculture) were simultaneously fitted to precisely estimate the parameters associated with inter-subject variability in the growth of N87 and GFP-MCF7 cells.

Step 2: The final systems PK-PD model for T-vc-MMAE (Figure-5) was used to simultaneously characterize all the TGI profiles from all three tumor models. It was assumed that all the variability associated with TGI profiles was stemming from the variable in the growth. Consequently, tumor doubling times and associated inter-subject variability were fixed, and only the common efficacy parameters (K_{max} , $KC50$, τ) pertaining to MMAE induced tumor cell killing were estimated.

Simulations for tumor growth profiles of N87 and GFP-MCF7 fractions in a heterogeneous model:

Once the full tumor PK-PD model (Fig. 5) was validated by characterizing the entire TGI dataset, simulations were performed to comparatively evaluate growth profiles of N87 and GFP-MCF7 fractions (within a heterogeneous tumor) in comparison to whole 50:50 coculture tumor after IV administration of 1 mg/Kg and 10 mg/Kg T-vc-MMAE. For these set of simulations, common estimated efficacy parameters and the mean doubling time parameters associated with N87 and GFP-MCF7 growth were utilized without consideration of any inter-subject variability.

Simulations for model-predicted ‘bystander effect’ following single or fractionated dosing regimen:

JPET Manuscript # 262287

Since the main mechanism of bystander effect is enhanced killing of antigen-low (GFP-MCF7) cells in the presence of antigen-high (N87) cells, this effect was investigated by performing simulations using the final PK-PD model. Tumor growth profiles for ‘MCF7 fraction’ of a heterogeneous tumor were simulated at 1-10 mg/kg doses, which were either administered as a single dose or in a fractionated dosing regimen (4 equal doses administered every 4 days, Q4dX4). The improvement in the efficacy against ‘MCF7 fraction’ of a heterogeneous tumor was analyzed to identify the dose or dosing regimen that leads to the maximum bystander effect. These set of simulations were performed without any inter-subject variability.

Effect of different fractionated dosing regimens on maximizing TGI of 50:50 coculture xenograft:

A clinically relevant dose of 3.6 mg/kg was selected, and its effect was evaluated on the TGI of a heterogeneous tumor with 50:50 composition of N87 and GFP-MCF7 cells. The selected dose (3.6 mg/kg) was either administered as a single IV dose or as a fractionated dose in the form of 1.2 mg/kg given Q4dX3 or 0.6 mg/kg given Q4dX6. Tumor growth profiles for the ‘whole’ heterogeneous tumor and its N87 and GFP-MCF7 fractions were simulated and compared with the control profiles.

Data analysis:

Initial model development and simulation work was performed using Berkeley Madonna® (University of California at Berkeley, CA). Model fitting to TGI profiles was accomplished using Stochastic Approximation Expectation Maximization (SAEM) algorithm in Monolix version 8 (Lixoft®) (Lavielle and Mentre, 2007).

JPET Manuscript # 262287

RESULTS

Immunohistochemical (IHC) analysis of the heterogeneous tumor:

Figure 1A shows a representative fluorescent image of the histological section of heterogeneous tumor. The experiment was done in triplicate, and (Supplementary Figure 1) shows the images of all three coculture tumors. Fluorescent images of DAPI (in blue) and GFP (in green) were merged to identify the regions of interest. It was observed that the intensity of GFP signal was highly variable and heterogeneous. There were regions of densely populated GFP-MCF7 cells (Figure A1), and the regions where DAPI signal was predominant (Figure A2), suggesting the presence of N87 cells. It was also observed that the two cell-types were not 'well-mixed' and grew in clusters. Figure 1B shows the results of semi-quantitative analysis of the sections by ImageJ software. The fluorescent images from DAPI and GFP were isolated, and percentage of the tumor area emitting each fluorescence signal was determined. It was observed that ~80 % of the total tumor area within the section was covered with tumor cells. In addition, it was observed that ~43% of the tumor area was covered with GFP-labeled MCF7 cells. As such, it was calculated that ~53% of the tumor cells were GFP-MCF7 cells. Based on these estimates a 50:50 composition of two cell-types was assumed in the coculture tumors for the modeling work.

Plasma and tumor pharmacokinetics of T-vc-MMAE:

Figure 2A depicts plasma PK profiles of total trastuzumab (2A1), total MMAE (2A2), and free MMAE (2A3) in all three tumor models using validated bioanalytical techniques (Supplementary Figures 16-17 and Tables S1-S4) . As shown in the figure, there was no notable difference between the plasma PK profiles in different tumor models, suggesting the presence of tumor does not significantly contribute towards systemic PK of ADC. Non-compartmental analysis (NCA) of the plasma PK profile of T-vc-MMAE in SCID mice has been reported by us earlier (Singh et al.,

JPET Manuscript # 262287

2019). Figure 2B depicts tumor PK of T-vc-MMAE in all three mouse models. It was observed that the tumor exposures of total trastuzumab (2B1), total MMAE (2B2), and free MMAE (2B3) was higher in HER2-high N87 xenografts compared to HER2-low GFP-MCF7 xenografts. Within the coculture tumor, it was observed that total Trastuzumab profile was very similar to HER2-high N87 tumors. However, free MMAE and total MMAE profiles initially started at the same exposure levels as GFP-MCF7 tumors, and then gradually reached to a level similar to N87 tumors, with a prolonged Tmax (time taken to achieve maximum exposure, Cmax) in comparison to both N87 and GFP-MCF7 tumors. Interestingly, at the last time point (168h) the exposure of free MMAE and total MMAE in 50:50 coculture tumors was higher than both N87 and GFP-MCF7 tumors. This may stem from the processing of ADCs in antigen-high cells, followed by the release of free drug in the extracellular space, which could then accumulate in the intact antigen-low cells.

Tumor growth inhibition (TGI) studies:

Figure 2C shows mean tumor growth profiles for N87, GFP-MCF7, and 50:50 coculture tumors. It was observed that although there was a considerable variability in the growth of individual tumors, in general N87 control tumors grew slower compared to GFP-MCF7 and 50:50 coculture control tumors. Since GFP-MCF7 cells are fast growing, one would expect that they would take-over the 50:50 coculture tumor over time. Consequently, the growth of 50:50 coculture tumors was similar (Fig. 2C1) to GFP-MCF7 tumors. Within the 3 mg/kg treatment group, it was observed that initially the growth inhibition for 50:50 coculture tumor was similar to N87 tumors, and once the killing signal diminished the coculture tumors grew at a faster rate similar to GFP-MCF7 tumors. In 5 mg/kg group as well, coculture tumors regressed faster than GFP-MCF7 tumors, but once the killing signal was diminished, they grew similar to GFP-MCF7 tumors. In the 10 mg/kg group (Figure 2C4), HER2-high N87 tumors declined much faster than coculture tumors, which

JPET Manuscript # 262287

in the beginning showed a profile similar to GFP-MCF7 tumors. However, the coculture tumors eventually showed a delayed decline at a level similar to N87 tumors, before growing back up at a rate similar to GFP-MCF7 tumors. This observation matches the tumor PK data generated at 10 mg/kg dose, where it was observed that MMAE exposure in the coculture tumors starts at the level like GFP-MCF7 tumors, but once the ADC is processed by N87 cells the exposure levels go up to N87 tumor levels. These data also accentuate the fact that a sustained presence of high antigen expressing cells is required to achieve prolonged bystander effect by ADCs.

Development of the systems PK-PD model to characterize *in vivo* bystander effect of ADC:

Plasma pharmacokinetic model for T-vc-MMAE:

Plasma PK profiles of all three analytes from all three mouse models was fitted simultaneously using our previously published integrated plasma PK model for ADCs. The model fitted profiles (Supplementary Figure 3) and relevant parameter values/estimates are provided in Table 1.

A priori prediction of tumor pharmacokinetics of T-vc-MMAE in a heterogeneous tumor:

In the past we have combined single cell disposition model of ADC with mechanistic tumor distribution model to characterize the exposure of different T-vc-MMAE analytes in GFP-MCF7 and N87 tumors (Singh and Shah, 2017b). All the parameters of this model were previously known or obtained from *in vitro* modeling (Singh and Shah, 2017b), and only the parameters related to the accessibility of HER2 receptors within the tumor were estimated. In the past, we have also presented the global sensitivity analysis of this model. Here we have expanded this model to account for tumor heterogeneity. All the parameters associated with plasma PK, tumor distribution, and cellular disposition of T-vc-MMAE were *a priori* known. Based on the semi-quantitative IHC analysis, composition of two cell-types within the heterogeneous tumor was assumed to be 50:50.

JPET Manuscript # 262287

Using the model shown in Figure 3A, equations described in the methods section, and known model parameters shown in Table 1, tumor exposure of the 3 T-vc-MMAE analytes in the heterogeneous tumor was *a priori* predicted. Figure 3B shows the predicted PK profiles superimposed over the observed data. It was found that the coculture PK model was able to *a priori* predict the exposure of different ADC analytes in the heterogeneous tumor reasonably well.

Simulation of free and total MMAE exposure at different dose-levels in the three tumor models:

The final model was used to simulate the effect of different ADC doses on tumor exposure of unconjugated and total MMAE. Simulations were performed at different dose-levels, ranging from 0.1-10 mg/kg. The model predicted (Supplementary Figure 4) sustained exposure and longer T_{max} of free and total MMAE in the coculture tumors, which mainly stems from the time taken by N87 cells to process T-vc-MMAE and redistribution of MMAE to bystanding cells.

Simulation of intracellular tubulin occupancy for each cell-type in the heterogeneous tumor:

Figure 4A shows simulated percentage tubulin occupancy by MMAE ($\text{Occ}_{\text{Tub}}^{\text{i}}$) for N87 and GFP-MCF7 cells in the 50:50 coculture tumor. Simulations were performed at 0.1, 1, and 10 mg/kg doses of T-vc-MMAE. It was observed that at lower doses the difference in tubulin occupancy between HER2-high N87 cell and HER2-low GFP-MCF7 cell was much higher, which is expected as most of the ADC molecules will gravitate towards antigen-positive cells at this dose level. As the dose increased, both the cells achieved very similar occupancy, which may be due to the saturation of antigen-mediated pathway. These simulations suggest that at lower doses T-vc-MMAE may preferentially kill N87 cells over GFP-MCF7 cells. Figure 4B shows simulated tubulin occupancy for GFP-MCF7 cells with increasing fraction of N87 cells in the coculture tumor. It was observed that irrespective of the ADC dose an increase in the fraction of N87 cells

JPET Manuscript # 262287

led to higher tubulin occupancy for GFP-MCF7 cells, which is consistent with the bystander effect phenomenon. Interestingly, it was observed that the improvement in tubulin occupancy was more prominent for 1 mg/kg dose compared to 0.1 or 10 mg/kg doses. This could be because at lower doses the availability of MMAE maybe limiting and at higher doses tubulin maybe close to saturation. As such, these simulations suggest that there could be a bell-shaped relationship between ADC dose and the beneficial effects of the bystander effect.

Characterization of TGI data using the systems PK-PD model:

Figure 6 shows individual model fittings for representative animals, whereas the fittings for all the animals along with goodness of fits (GoF) plots and visual predictive checks (VPCs) are provided in supplementary data (Supplementary Figures 5-13). The population PK-PD model was able to simultaneously characterize all the TGI data reasonably well, as highlighted by the GoF plots (Supplementary Figures 10-11), as well as prediction-corrected VPCs (Supplementary Figures 13). The doubling times for N87 and GFP-MCF7 tumors were estimated with good precision and were found to be 13.6 and 9.1 days respectively, with ~30% inter-subject variability on each parameter (Table 1). The efficacy for each cell-type was driven using a killing function, which utilized common PD parameters (K_{max} , $KC50$, τ) to induce intracellular tubulin occupancy mediated cell cytotoxicity. Model estimated *in vivo* K_{max} and $KC50$ values of $0.4 \frac{1}{day}$ and 99.8 % were very similar to *in vitro* estimated vales for MMAE induced cell killing (K_{max} of $0.72 \frac{1}{day}$, and $KC50$ of 98.3 % for N87 cells and 96.1% for GFP-MCF7 cells) (Singh and Shah, 2019).

Simulations for growth profiles of N87 and GFP-MCF7 tumor fractions:

The final PK-PD model was used to investigate the dynamics of N87 and GFP-MCF7 tumor fractions within the coculture tumor, after treatment with different doses of T-vc-MMAE. It was

JPET Manuscript # 262287

observed (Supplementary Figure 11) that in the beginning the whole tumor declines in parallel to a decline in N87 and GFP-MCF7 fractions of the tumor. However, when the tumor starts to regrow the majority of tumor fraction comprised of GFP-MCF7 cells, which are less responsive to the ADC and shows a faster growth pattern.

Simulations to investigate the effect of fractionated dosing regimen on bystander effect of ADC in a heterogeneous tumor:

These simulations were performed to investigate how the rate and extent of bystander effect changes with varying ADC dose-levels, dosing regimens, and compositions of the heterogeneous tumors. Figure 7 provides the results from these simulations, in the form of ‘MCF7 fraction’ tumor volume changes with time. In the single dose group, it was observed that an increase in % of N87 fraction in the heterogeneous tumor led to higher killing of MCF7 cells, especially at the lower dose. This observation is consistent with the expected enhancement of ADC bystander effect with an increase in the fraction of antigen-positive cells. When the ADC doses were fractionated, it was observed that fractionated dosing regimen was more efficacious in killing 100% MCF tumors and ‘MCF7 fractions’ in the coculture tumors. This effect was also more prominent at lower dose levels of ADC. These simulations suggest that fractionated dosing regimen maybe more beneficial in achieving sustaining tubulin occupancy within antigen negative tumor cells. In addition, it was observed that as the % of N87 fraction increased beyond certain level (i.e. 50%), there was no further improvement in the bystander killing by the ADC, even in the presence of the fractionated dosing regimen.

Within the simulation results (Supplementary Figure 14-15) for the fractionated dosing regimen in the form of ‘total’ tumor volume (along with each cell-type fraction) changes with time, it was observed that in comparison to the single dose fractionated dosing regimen leads to an

JPET Manuscript # 262287

improvement in the efficacy of ADC for the heterogeneous tumor. Majority of this improvement stemmed from enhanced killing of N87 tumor fraction, which in turn contributed to higher killing of GFP-MCF7 fraction of the tumor via the bystander effect.

JPET Manuscript # 262287

DISCUSSION

A systems PK-PD model that can characterize *in vivo* bystander effect of ADCs in heterogeneous solid tumors could significantly improve the discovery and development of clinically successful ADCs. Towards this goal we have taken a stepwise approach of conducting experiments and building systems models (Supplementary Figure 2). Current investigation represents the final step of this process that requires *in vivo* experiments in a heterogeneous tumor model. The heterogeneous tumor model was developed by inoculating a mixture of GFP-MCF7 and N87 cells in the mice. Since both the cells have different growth rates, after several attempts, a ratio of ~1 million GFP-MCF7 and ~9 million N87 cells was finalized to obtain a coculture composition of 50:50 at tumor volumes ~350-400 mm³. This coculture composition was confirmed by semi-quantitative IHC analysis (Figure 1).

A detailed PK and TGI study were conducted on the heterogeneous tumors using our tool ADC, T-vc-MMAE (Figure 2). PK-PD data generated using the heterogeneous tumor bearing mice were also compared with the data from 100% N87 and GFP-MCF7 tumor bearing mice. It was observed that there was no difference in the plasma PK of different ADC analytes between the three tumor models. This result suggests that presence of tumor did not significantly affect systemic PK of ADC, and confirms our previous observation that the amount of payload coming from the tumor space does not contribute significantly towards overall systemic PK of the drug (Shah et al., 2014). Tumor PK data revealed that coculture tumors had prolonged exposure of free and total MMAE compared to GFP-MCF7 and N87 tumors. We hypothesize that this may stem from the fact that it takes time for N87 (Ag+) cells to first process the ADC and release the free MMAE in the tumor extracellular space, which subsequently redistributes and accumulate into the bystanding GFP-MCF7 (Ag-) cells.

JPET Manuscript # 262287

Tumor growth data revealed that 50:50 coculture tumors grew at a rate similar to the fast growing GFP-MCF7 tumors, suggesting faster growing cells within a heterogeneous tumor will eventually take over most of the tumor in the absence of any treatment. TGI data revealed that the efficacy of ADC in 50:50 coculture tumors was always higher than the GFP-MCF7 tumors, and this enhanced efficacy persisted unless there was a regrowth following ablation of N87 cells. This observation accentuated the fact that killing of N87 cells was important to exert the bystander effect in GFP-MCF7 cells (Singh et al., 2016b), however, once the N87 cells are ablated there won't be any bystander effect and the coculture tumors will start growing at the rate similar to GFP-MCF7 tumors. As such, an ideal ADC and dosing regimen should lead to a parallel decline in antigen-positive and antigen-negative cells within a heterogeneous tumor.

In order to develop the systems PK-PD model for ADC, first our previously published tumor PK model was expanded to include two different population of cells growing at distinct growth rates. All the parameters associated with plasma PK, tumor distribution, and cellular PK of ADC in each cell-type were fixed to our previously reported values. The final tumor disposition model (Figure 3) was able to *a priori* predict tumor PK of all ADC analytes. The PK model also successfully predicted delayed T_{max} associated with the exposure of total and free MMAE in the coculture tumors compared to N87 and GFP-MCF7 tumors (Supplementary Figure 4). The model was also used to simulate tubulin occupancy in different cell-types within the heterogeneous tumor at different dose-levels (Figure 4). It was observed that the difference in tubulin occupancy between the two cells was more pronounced at lower doses, where N87 cells showed higher occupancy compared to GFP-MCF7 cells. These simulations corroborated TGI data where higher ADC efficacy was observed for N87 tumors compared to GFP-MCF7 tumors, and also supported our approach of utilizing tubulin occupancy by MMAE as a driver for ADC efficacy (Singh and Shah,

JPET Manuscript # 262287

2019). Effect of heterogeneous tumor composition on tubulin occupancy was also simulated using the PK model. It was found that with increasing fraction of N87 cells in the tumor there was an increase in tubulin occupancy of GFP-MCF7 cells, which was consistent with the expectation of ADC bystander effect. However, simulations revealed that the extent of improvement in tubulin occupancy of GFP-MCF7 cells was dose dependent, and there may be a bell-shaped relationship between ADC dose and the improvement in bystander effect following enhancement of Ag⁺ cell fraction in a heterogeneous tumor. However, this hypothesis needs to be validated using experimental data.

The heterogeneous tumor PK model was integrated with a PD model to make the final systems PK-PD model (Figure 5), which utilized intracellular occupancy of tubulin as the driver of ADC efficacy. The final model was able to simultaneously characterize all the TGI data reasonably well, using a single set PD (K_{max} , KC_{50} , τ) parameters. In addition, the parameter estimates obtained from *in vivo* efficacy studies were very similar to previously obtained parameters from *in vitro* estimates (Singh and Shah, 2019). This observation highlights the importance of adopting a systems approach and suggests a good correlation between *in vitro* and *in vivo* efficacy of ADCs. The system PK-PD model was used to investigate the effect of ADC dose and increasing percentage of Ag⁺ cell fraction on the growth of Ag⁻ cell fraction. It was observed that the bystander effect of ADC was most optimal at 1-5 mg/kg doses, beyond which the effect seemed to saturate. Additionally, it was observed that having certain fraction of Ag⁺ cells (e.g. 50%) within the heterogeneous tumor would be enough to achieve the maximum bystander effect of ADC. The PK-PD model was also used to investigate the effect of fractionated dosing regimen on the efficacy of ADC in a heterogeneous tumor (Figure 7 and 8). Model simulations revealed that dose-fractionation may further improve overall efficacy and bystander effect of T-vc-MMAE, as it will

JPET Manuscript # 262287

prolong the duration of tubulin occupancy in each cell-type. While this is an exciting finding, it needs to be corroborated by experimental results, and the readers should be cautious before generalizing it to other ADCs and tumors. Nonetheless, the systems PK-PD model presented here for characterizing *in vivo* bystander effect of ADC in a heterogeneous tumor remains generalizable.

In summary, here we have presented a novel systems PK-PD model for ADCs that accounts for multiple populations of tumor cells. The model could account for differential exposures of ADC in each cell-type and can simultaneously characterize ADC-induced direct killing and bystander effect. Since the modeling paradigm presented here is formulated on a single-cell level, it could also be extended to other therapeutic scenarios where a molecule interacts with multiple cell-types within a tumor microenvironment (e.g. bi-specifics interacting with tumor and immune cells). Going forward we plan to translate this systems PK-PD to predict bystander effect of ADCs in the clinic (Shah et al., 2012; Betts et al., 2016; Singh and Shah, 2017a).

JPET Manuscript # 262287

ACKNOWLEDGEMENTS

Authors would like to acknowledge Dr. Sharad Sharma and Shabkaiz Masih for their help in development of analytical techniques and establish tumor models. Authors would also like to acknowledge Dr. Wade Sigurdson from School of Medicine and Biomedical Sciences, University at Buffalo, for his helpful assistance with fluorescent microscopy imaging of tumor samples. Authors would also like to acknowledge Zhe Li and David Bussing for their helpful assistance when needed, while executing certain experiments.

JPET Manuscript # 262287

AUTHORS' CONTRIBUTION:

Participated in research design: Singh, Shah

Conducted experiments: Singh, Siegal, Guo, Verma, Wong, Chang

Performed data analysis: Singh, Siegal, Shah

Wrote or contributed to the writing of the manuscript: Singh, Shah

JPET Manuscript # 262287

References

- Anthony L KR (2018) Review of the ADC Clinical Pipeline, in *World ADC Summit*, Berlin.
- Betts AM, Haddish-Berhane N, Tolsma J, Jasper P, King LE, Sun Y, Chakrapani S, Shor B, Boni J and Johnson TR (2016) Preclinical to Clinical Translation of Antibody-Drug Conjugates Using PK/PD Modeling: a Retrospective Analysis of Inotuzumab Ozogamicin. *AAPS J* **18**:1101-1116.
- Cilliers C, Guo H, Liao J, Christodolu N and Thurber GM (2016) Multiscale Modeling of Antibody-Drug Conjugates: Connecting Tissue and Cellular Distribution to Whole Animal Pharmacokinetics and Potential Implications for Efficacy. *AAPS J* **18**:1117-1130.
- Donoghue JF, McGavigan CJ, Lederman FL, Cann LM, Fu L, Dimitriadis E, Girling JE and Rogers PA (2012) Dilated thin-walled blood and lymphatic vessels in human endometrium: a potential role for VEGF-D in progestin-induced break-through bleeding. *PLoS One* **7**:e30916.
- Khot A, Sharma S and Shah DK (2015) Integration of bioanalytical measurements using PK-PD modeling and simulation: implications for antibody-drug conjugate development. *Bioanalysis* **7**:1633-1648.
- Kovtun YV, Audette CA, Ye Y, Xie H, Ruberti MF, Phinney SJ, Leece BA, Chittenden T, Blattler WA and Goldmacher VS (2006) Antibody-drug conjugates designed to eradicate tumors with homogeneous and heterogeneous expression of the target antigen. *Cancer Res* **66**:3214-3221.
- Lambert JM (2015) Antibody-Drug Conjugates (ADCs): Magic Bullets at Last! *Mol Pharm* **12**:1701-1702.

JPET Manuscript # 262287

- Lavielle M and Mentre F (2007) Estimation of population pharmacokinetic parameters of saquinavir in HIV patients with the MONOLIX software. *J Pharmacokinet Pharmacodyn* **34**:229-249.
- Mantaj J, Jackson PJ, Rahman KM and Thurston DE (2017) From Anthramycin to Pyrrolobenzodiazepine (PBD)-Containing Antibody-Drug Conjugates (ADCs). *Angew Chem Int Ed Engl* **56**:462-488.
- Monte UD (2009) Does the cell number 10^9 still really fit one gram of tumor tissue? *Cell Cycle* **8**:505-506.
- Ogitani Y, Hagihara K, Oitate M, Naito H and Agatsuma T (2016) Bystander killing effect of DS-8201a, a novel anti-human epidermal growth factor receptor 2 antibody-drug conjugate, in tumors with human epidermal growth factor receptor 2 heterogeneity. *Cancer Sci* **107**:1039-1046.
- Schneider CA, Rasband WS and Eliceiri KW (2012) NIH Image to ImageJ: 25 years of image analysis. *Nature Methods* **9**:671.
- Seol H, Lee HJ, Choi Y, Lee HE, Kim YJ, Kim JH, Kang E, Kim SW and Park SY (2012) Intratumoral heterogeneity of HER2 gene amplification in breast cancer: its clinicopathological significance. *Mod Pathol* **25**:938-948.
- Shah DK, Haddish-Berhane N and Betts A (2012) Bench to bedside translation of antibody drug conjugates using a multiscale mechanistic PK/PD model: a case study with brentuximab-vedotin. *J Pharmacokinet Pharmacodyn* **39**:643-659.
- Shah DK, King LE, Han X, Wentland JA, Zhang Y, Lucas J, Haddish-Berhane N, Betts A and Leal M (2014) A priori prediction of tumor payload concentrations: preclinical case study with an auristatin-based anti-5T4 antibody-drug conjugate. *AAPS J* **16**:452-463.

JPET Manuscript # 262287

- Singh AP, Guo L, Verma A, Wong GG and Shah DK (2019) A Cell-Level Systems PK-PD Model to Characterize In Vivo Efficacy of ADCs. *Pharmaceutics* **11**.
- Singh AP, Krzyzanski W, Martin SW, Weber G, Betts A, Ahmad A, Abraham A, Zutshi A, Lin J and Singh P (2015a) Quantitative prediction of human pharmacokinetics for mAbs exhibiting target-mediated disposition. *AAPS J* **17**:389-399.
- Singh AP, Maass KF, Betts AM, Wittrup KD, Kulkarni C, King LE, Khot A and Shah DK (2016a) Evolution of Antibody-Drug Conjugate Tumor Disposition Model to Predict Preclinical Tumor Pharmacokinetics of Trastuzumab-Emtansine (T-DM1). *AAPS J* **18**:861-875.
- Singh AP and Shah DK (2017a) Application of a PK-PD Modeling and Simulation-Based Strategy for Clinical Translation of Antibody-Drug Conjugates: a Case Study with Trastuzumab Emtansine (T-DM1). *AAPS J* **19**:1054-1070.
- Singh AP and Shah DK (2017b) Measurement and Mathematical Characterization of Cell-Level Pharmacokinetics of Antibody-Drug Conjugates: A Case Study with Trastuzumab-vc-MMAE. *Drug Metab Dispos* **45**:1120-1132.
- Singh AP and Shah DK (2018) Utility of PK-PD Modeling and Simulation to Improve Decision Making for Antibody-Drug Conjugate Development, in *Innovations for Next-Generation Antibody-Drug Conjugates Cancer Drug Discovery and Development* (Damelin M ed), Humana Press, Cham.
- Singh AP and Shah DK (2019) A "Dual" Cell-Level Systems PK-PD Model to Characterize the Bystander Effect of ADC. *J Pharm Sci*.
- Singh AP, Sharma S and Shah DK (2016b) Quantitative characterization of *in vitro* bystander effect of antibody-drug conjugates. *J Pharmacokinet Pharmacodyn* **43**:567-582.

JPET Manuscript # 262287

- Singh AP, Shin YG and Shah DK (2015b) Application of Pharmacokinetic-Pharmacodynamic Modeling and Simulation for Antibody-Drug Conjugate Development. *Pharm Res* **32**:3508-3525.
- Thurber GM, Schmidt MM and Wittrup KD (2008a) Antibody tumor penetration: transport opposed by systemic and antigen-mediated clearance. *Adv Drug Deliv Rev* **60**:1421-1434.
- Thurber GM, Schmidt MM and Wittrup KD (2008b) Factors determining antibody distribution in tumors. *Trends Pharmacol Sci* **29**:57-61.
- van Geel R, Wijdeven MA, Heesbeen R, Verkade JM, Wasiel AA, van Berkel SS and van Delft FL (2015) Chemoenzymatic Conjugation of Toxic Payloads to the Globally Conserved N-Glycan of Native mAbs Provides Homogeneous and Highly Efficacious Antibody-Drug Conjugates. *Bioconjug Chem* **26**:2233-2242.
- Yang J, Mager DE and Straubinger RM (2010) Comparison of two pharmacodynamic transduction models for the analysis of tumor therapeutic responses in model systems. *AAPS J* **12**:1-10.

JPET Manuscript # 262287

CONFLICT OF INTEREST:

Authors declare no conflict of interest

JPET Manuscript # 262287

FIGURE LEGENDS

Figure 1: Imaging analysis of coculture tumors grown using a mixture of N87 and GFP-MCF7 cells and harvested at a volume of ~350-400 mm³. **(A)** A representative image of the middle section of the tumor. The green signal represents GFP-transfected MCF7 cells, and the blue signal from DAPI represent nucleus of all tumor cells. *(A1)* A zoomed region of the tumor populated with GFP-MCF7 cells, which have both ‘green’ and ‘blue’ signals. *(A2)* A zoomed region of the tumor populated with N87 cells, which have only ‘blue’ signal. **(B)** A quantitative analysis of the middle sections of three tumors to calculate the percentage of GFP-MCF7 cells within a heterogeneous tumor.

Figure 2: **(A)** Plasma PK of all three ADC analytes in GFP-MCF7, N87, and coculture tumor bearing mice, after 10 mg/kg intravenous dose of T-vc-MMAE. *(A1)* total Trastuzumab, *(A2)* total MMAE, and *(A3)* free MMAE. **(B)** Tumor PK of all three ADC analytes in GFP-MCF7, N87, and coculture tumor bearing mice, after 10 mg/kg intravenous dose of T-vc-MMAE. *(B1)* total trastuzumab, *(B2)* total MMAE, and *(B3)* free MMAE. **(C)** Tumor growth profiles for all three xenograft models. *(C1)* control, *(C2)* 3 mg/kg T-vc-MMAE, *(C3)* 5 mg/kg T-vc-MMAE, and *(C4)* 10 mg/kg T-vc-MMAE.

Figure 3: **(A)** A schematic diagram of a systems pharmacokinetic model developed to characterize T-vc-MMAE PK in a heterogeneous tumor containing N87 and GFP-MCF7 cells. Plasma PK: Disposition of T-vc-MMAE in systemic and peripheral spaces is characterized using a 2-compartment model with linear clearance from the central compartment. Processes associated with non-specific deconjugation of MMAE and catabolic clearance of T-vc-MMAE contribute to the formation of free MMAE, which is also characterized using a 2-compartment model with distribution to peripheral tissues and linear clearance from the central compartment. Tumor

JPET Manuscript # 262287

Distribution: Distribution of T-vc-MMAE and free MMAE from the central compartment to tumor extracellular space was assumed to be driven by two diffusive processes: surface and vascular exchange. *Single Cell Disposition in two cell-types:* Once in the extracellular space, T-vc-MMAE was assumed to distribute to both N87 and GFP-MCF7 cells, which have distinct growth rates. Once bound to HER2 receptors on the cell, T-vc-MMAE can internalize into endosomal/lysosomal space of each cell. Upon enzymatic degradation and linker cleavage, free MMAE is released in the cytoplasmic space, which can either bind to intracellular tubulin or freely exchange within the extracellular space using influx and efflux rates. Once in tumor extracellular space, free MMAE can either distribute to other cells or diffuse out into the systemic circulation. **(B)** *A priori* predictions made by the tumor PK model for all three ADC analytes in the three tumor models. *(B1)* total MMAE, *(B2)* free MMAE, and *(B3)* total trastuzumab.

Figure 4: **(A)** Simulations for intracellular occupancy of tubulin by MMAE (Occ_{Tub}) for GFP-MCF7 (profiles in green) and N87 (profiles in red) cell in the 50:50 coculture tumor, after single intravenous dose of 0.1, 1, and 10 mg/kg T-vc-MMAE. **(B)** Simulations for improvement in tubulin occupancy of GFP-MCF7 cell ($\text{Occ}_{\text{Tub}}^{\text{MCF7}}$) after increasing percentages of N87 cell fraction within the heterogeneous tumor. Simulations were performed at 0.1, 1, and 10 mg/kg dose of T-vc-MMAE.

Figure 5: Schematic diagram of the full systems PK-PD model developed to characterize bystander effect of T-vc-MMAE in a heterogeneous tumor containing N87 and GFP-MCF7 cells. The plasma and tumor pharmacokinetics, as well as disposition of T-vc-MMAE in each cell-type, is similar to Figure 3. Intracellular occupancy of tubulin by MMAE (Occ_{Tub}) in each cell-type was assumed to drive the efficacy of ADC, which was characterized by shuttling of growing cells into non-growing phases destined to die. It was assumed that growing and non-growing cells contribute

JPET Manuscript # 262287

towards the disposition of T-vc-MMAE and free MMAE. When the cells die, intracellular content was assumed to release in tumor extracellular space and allowed to freely exchange with other living cells or systemic circulation.

Figure 6: Representative observed, and model fitted tumor growth profiles for GFP-MCF7 (green), N87 (red), and coculture (orange) tumors. (A) Control group, (B) 1 mg/kg, (C) 3 mg/kg, (D) 5 mg/kg, and (E) 10 mg/kg T-vc-MMAE. Individual fits for all animals as well as goodness of fit (GoF) plots (Supplementary Figures 5-10).

Figure 7: Simulations for the growth of ‘MCF7 fraction’ of a coculture tumor with varying percentage of N87 cells. Four different dose-levels of T-vc-MMAE were evaluated: 1, 3, 5, and 10 mg/kg, administered either as a single dose (left panels) or fractionated into 4 equal doses administered every 4 days (Q4dX4, right panels). (A1 and B1) 0% N87, (A2 and B2) 25% N87, (A3 and B3) 50% N87, (A4 and B4) 75% N87, and (A5 and B5) 90% N87 cells.

Figure 8: Comparative evaluation of tumor growth inhibition (TGI) of (A) 50:50 coculture tumor, (B) N87 fraction of the tumor, or (C) GFP-MCF7 fraction of the tumor, after single 3.6 mg/kg dose of ADC or fractionated dosing regimens of 1.2 mg/kg given Q4dX3 or 0.6 mg/kg Q4dX6.

JPET Manuscript # 262287

Table 1: A list of literature derived, or model estimated parameters used for the systems PK-PD model of T-vc-MMAE

Parameter	Definition	Value (CV %)	Unit	Source
Parameters associated with plasma pharmacokinetics of T-vc-MMAE				
CL_{ADC}, CLD_{ADC}	Central and distributional clearances of T-vc-MMAE	0.033 (4.8%), 0.0585 (12.6 %)	L/day/Kg	(Singh et al., 2019)
$V1_{ADC}, V2_{ADC}$	Central and peripheral volumes of distribution for T-vc-MMAE	0.084 (7.3%), 0.051 (5.2%)	L/Kg	Estimated (Singh et al., 2019)
CL_{Drug}, CLD_{Drug}	Central and distributional clearances of free MMAE	18.40, 1.84	L/day/Kg	(Shah et al., 2012)
$V1_{Drug}, V2_{Drug}$	Central and peripheral volumes of distribution for T-vc-MMAE	0.136, 0.523	L/Kg	(Shah et al., 2012)
K_{dec}^P	Non-specific deconjugation of MMAE from T-vc-MMAE	0.323 (8.8%)	1/day	(Singh et al., 2019)
Parameters associated with tumor distribution of T-vc-MMAE				
R_{Cap}	Radius of the tumor blood capillary	8.0	μm	(Shah et al., 2012; Shah et al., 2014; Singh et al., 2016a)
R_{Krogh}	An average distance between two capillaries	75.0	μm	(Shah et al., 2012; Shah et al., 2014; Singh et al., 2016a)
P_{ADC}, P_{Drug}	The rates of permeability of T-vc-MMAE and MMAE across the blood vessels respectively	334, 21000	$\mu m/day$	(Shah et al., 2012; Shah et al., 2014; Singh et al., 2016a)
D_{ADC}, D_{Drug}	The rates of diffusion of T-vc-MMAE and MMAE across the blood vessels respectively	0.022, 0.25	cm^2/day	(Shah et al., 2012; Shah et al., 2014; Singh et al., 2016a)
$\epsilon_{ADC}, \epsilon_{Drug}$	Tumor void volume for T-vc-MMAE and MMAE	0.24, 0.44	Unitless	(Shah et al., 2012; Shah et al., 2014; Singh et al., 2016a)
R_{Tumor}	Radius of a spherical tumor calculated based on varying tumor volume (TV) where:	Dynamic	cm	Calculated

JPET Manuscript # 262287

$$TV(t) = \frac{4}{3} * \pi * R^3_{\text{Tumor}}$$

Parameters associated with single cell disposition of T-vc-MMAE

K_{on}^{ADC}	2 nd order association rate constant between T-vc-MMAE and HER2 receptor	0.03	1/nM/h	(Singh and Shah, 2017b)
K_{off}^{ADC}	1 st order dissociation rate constant between T-vc-MMAE and HER2 receptor	0.014	1/h	(Singh and Shah, 2017b)
K_{int}^{ADC}	Internalization rate of HER2-ADC complex inside the cell	0.11	1/h	(Singh and Shah, 2017b)
K_{deg}^{ADC}	Intracellular degradation of T-vc-MMAE in endosomal/lysosomal space	0.353	1/h	(Singh and Shah, 2017b)
K_{on}^{Tub}	2 nd order association rate constant between cytoplasmic MMAE and intracellular tubulin protein	0.0183	1/nM/h	(Singh and Shah, 2017b)
K_{off}^{Tub}	1 st order dissociation rate constant between MMAE-tubulin complex	0.545	1/h	(Singh and Shah, 2017b)
Tub^{tot}	Total concentration of intracellular tubulin in a single cell	65	nM	(Shah et al., 2012)
K_{in}^{Drug}	1 st order influx rate of MMAE from extracellular to intracellular space	8.33	1/h	(Singh and Shah, 2017b)
K_{out}^{Drug}	1 st order efflux rate of MMAE from intracellular to extracellular space	0.046	1/day	(Singh and Shah, 2017b)
Ag_{N87}^{ex}, Ag_{MCF7}^{ex}	Model estimated HER2 receptor count on each tumor cell in N87 and GFP-MCF7 tumors <i>in vivo</i>	185,000 (2.8%), 22,400 (3.2%)	Numbers/Cell	(Singh et al., 2019)

Common estimated parameters associated with single cell killing in three mouse models

Kmax	1 st order killing rate of MMAE in each tumor cell (either GFP-MCF7 or N87) within 3 mouse models	0.41 (3.42%)	1/day	Estimated
KC50	Percentage of intracellular occupancy to tubulin by MMAE	99.8 (38.3%)	Percentage	Estimated

JPET Manuscript # 262287

which leads to 50% of maximum killing

τ	Transit time associated with MMAE induced killing	1.44 (8.3%)	Day	Estimated
γ	Curve-fitting parameter associated with sigmoidal tubulin occupancy-killing relationship	4.3 (48.6 %)	Unitless	Estimated
DT^{N87}, DT^{MCF7}	Doubling time of N87 and GFP-MCF7 tumor fractions	13.61 (6.3%), 9.13 (12.4%)	Day	Estimated
$IV^{DT^{N87}}, IV^{DT^{MCF7}}$	Inter-subject variability associated with doubling times of N87 and MCF7 tumor fractions assuming log-normal distribution	31.96% (13.12%), 29.3% (3.11%)	Percentage	Estimated

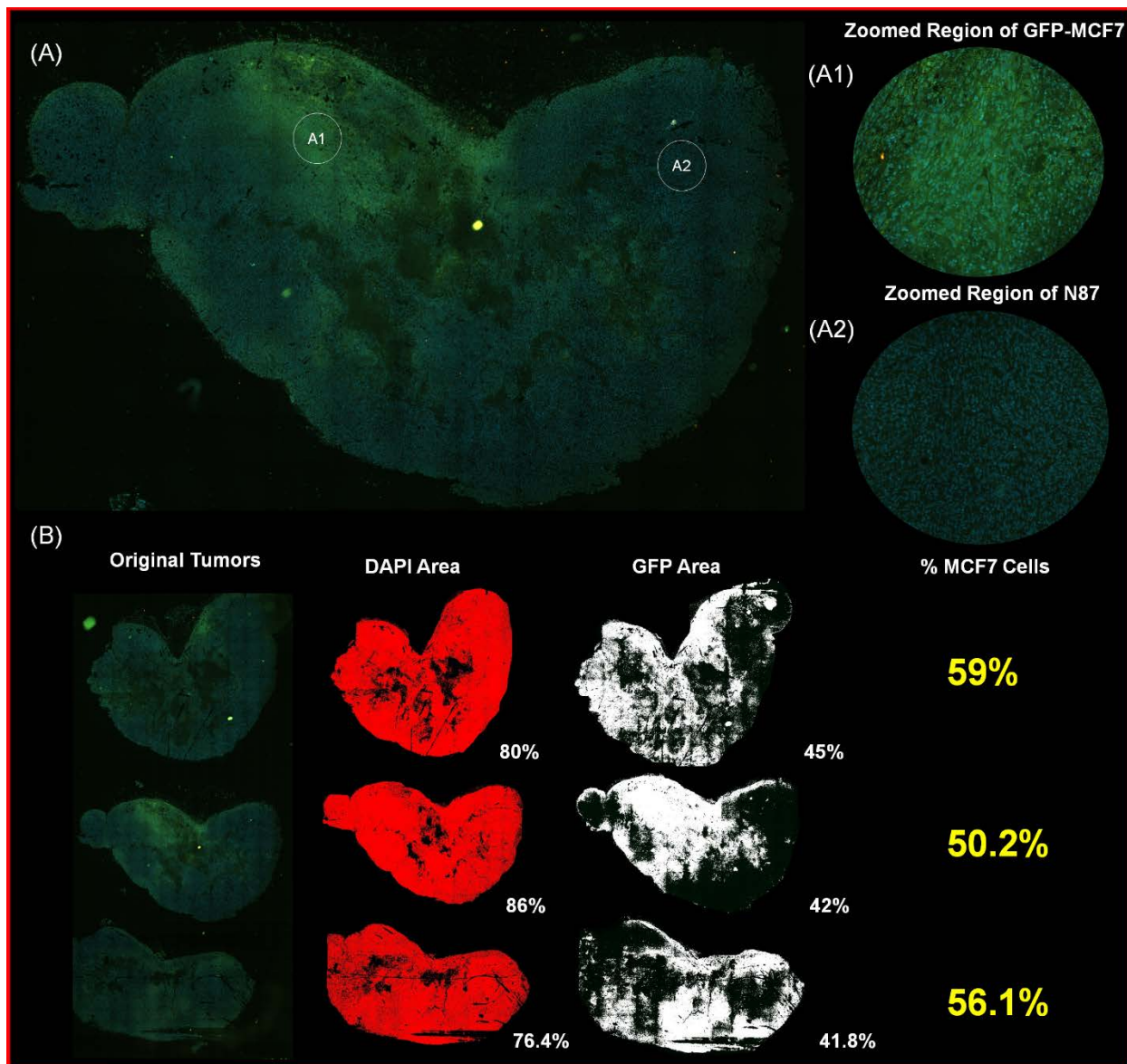


Figure 1

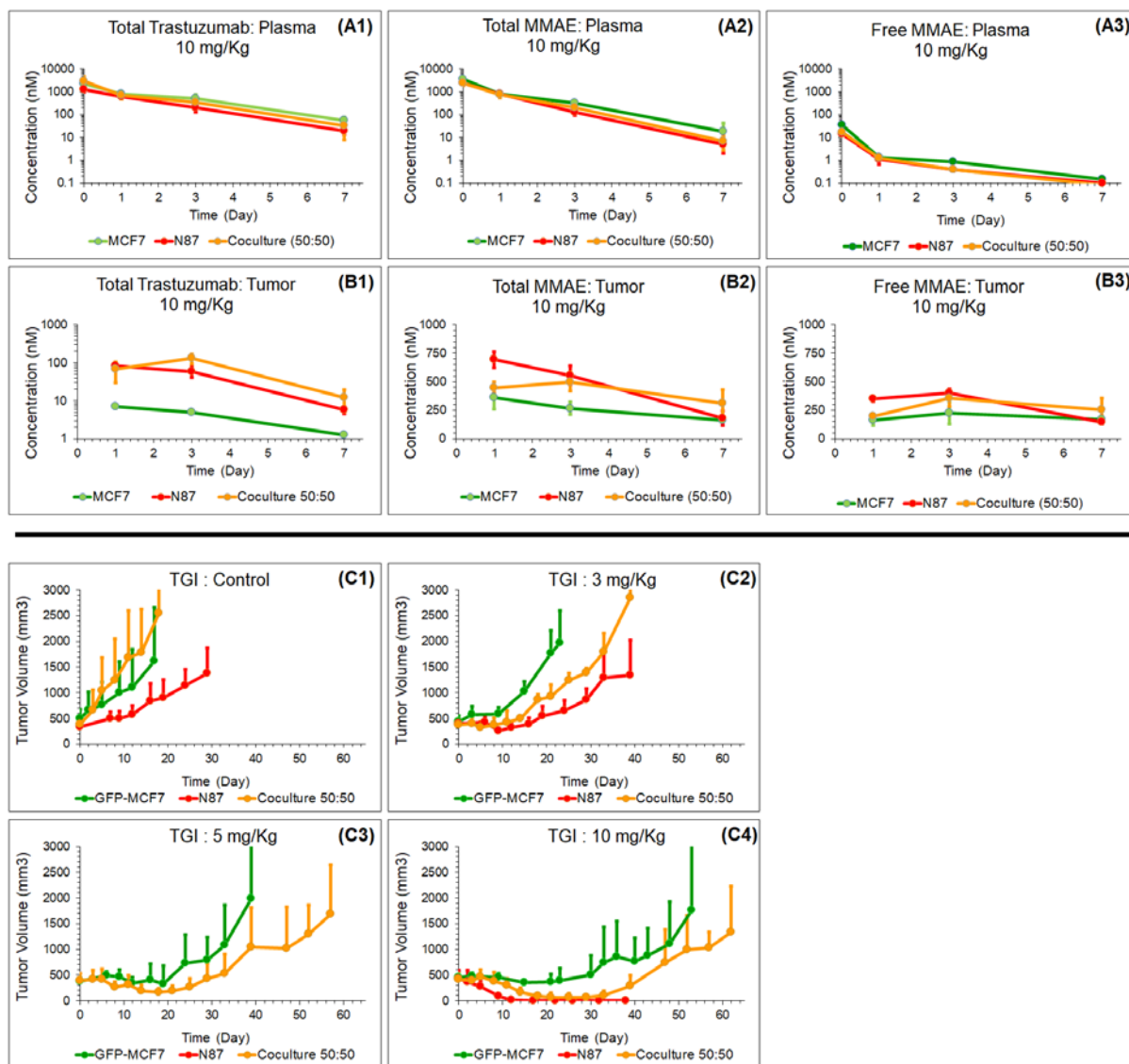


Figure 2

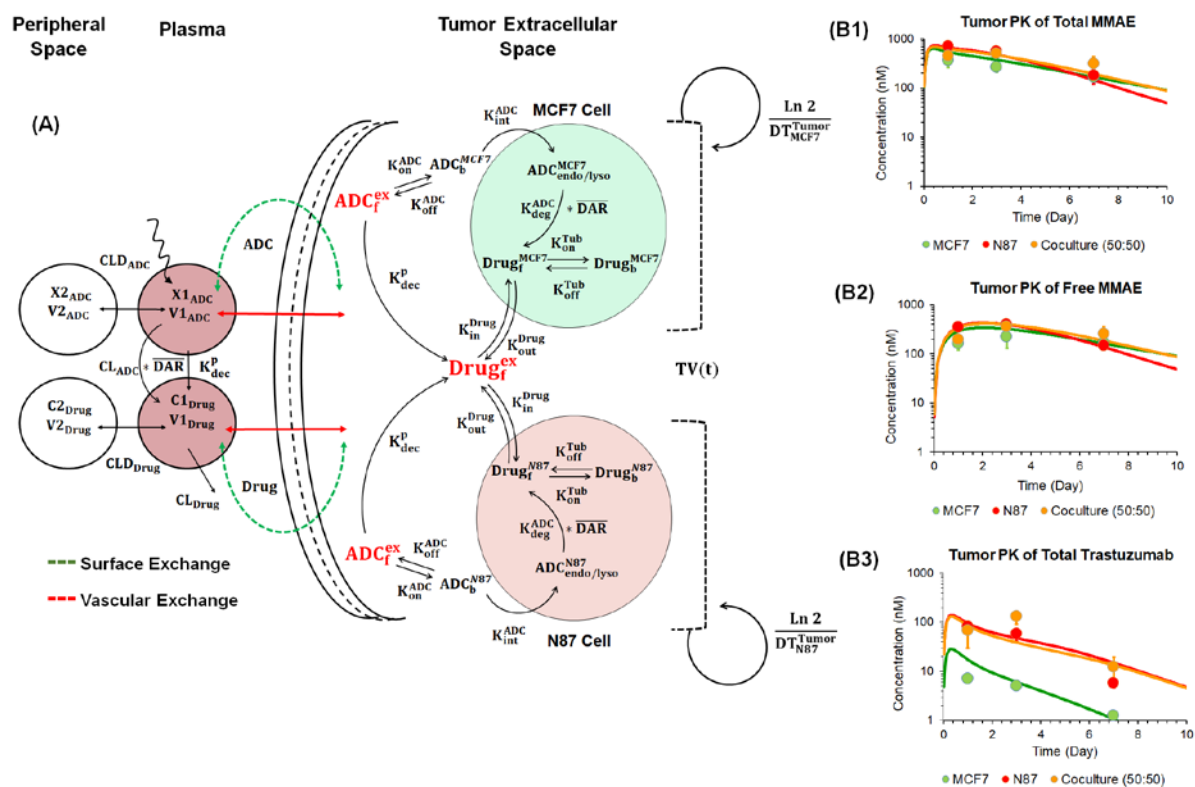


Figure 3

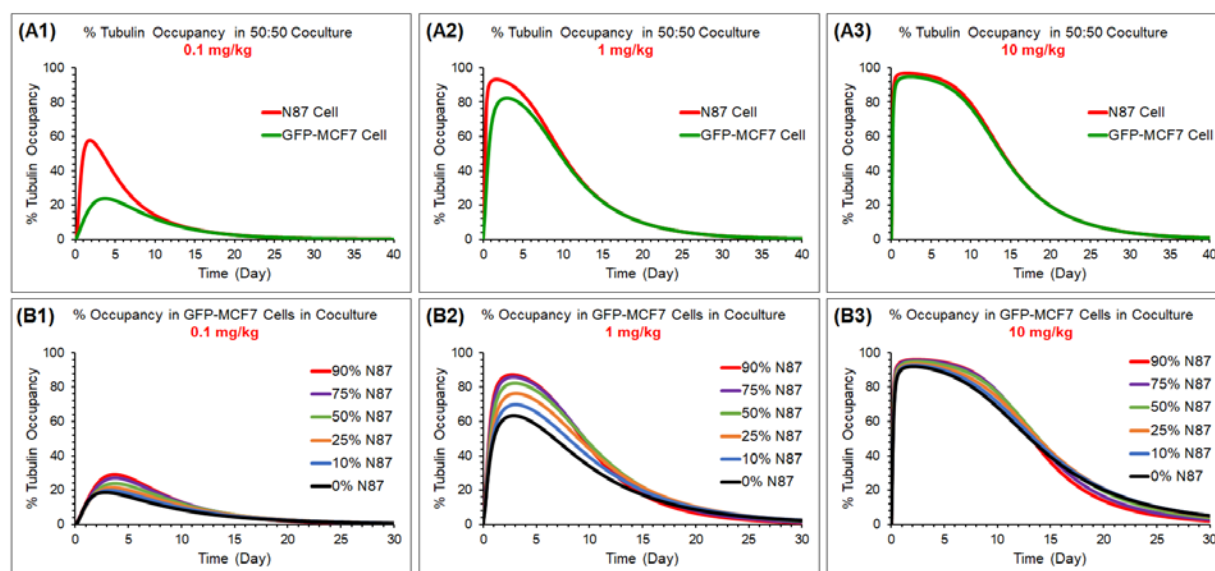


Figure 4

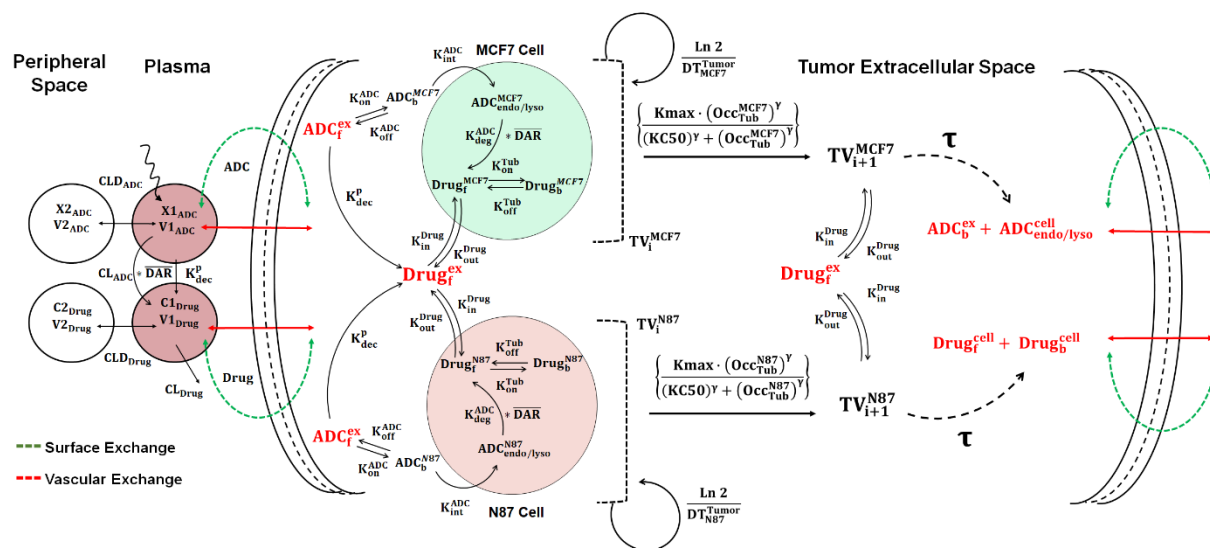
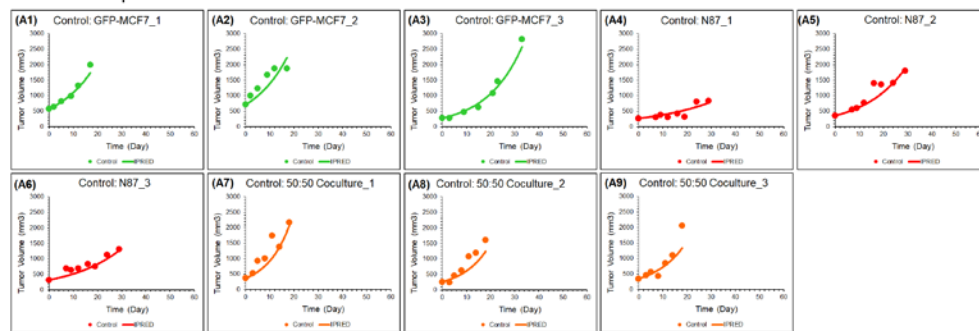
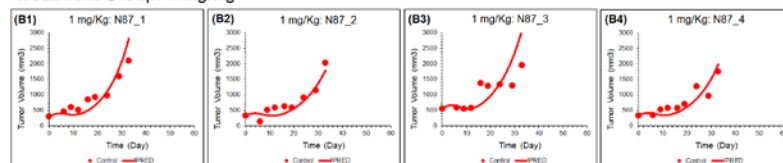


Figure 5

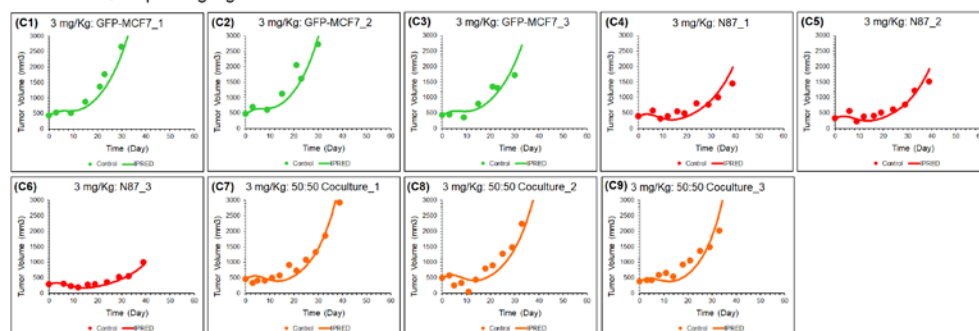
Control Group



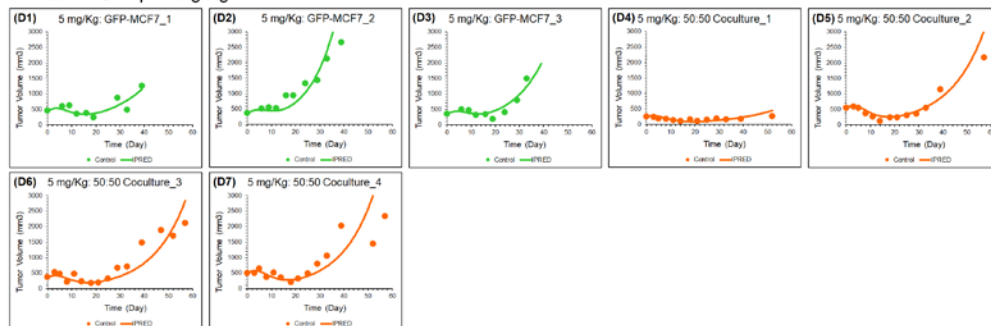
Treatment Group: 1 mg/Kg



Treatment Group: 3 mg/Kg



Treatment Group: 5 mg/Kg



Treatment Group: 10 mg/Kg

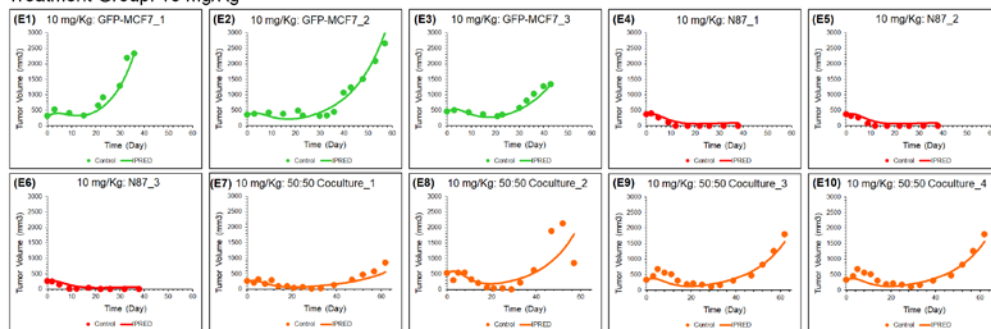


Figure 6

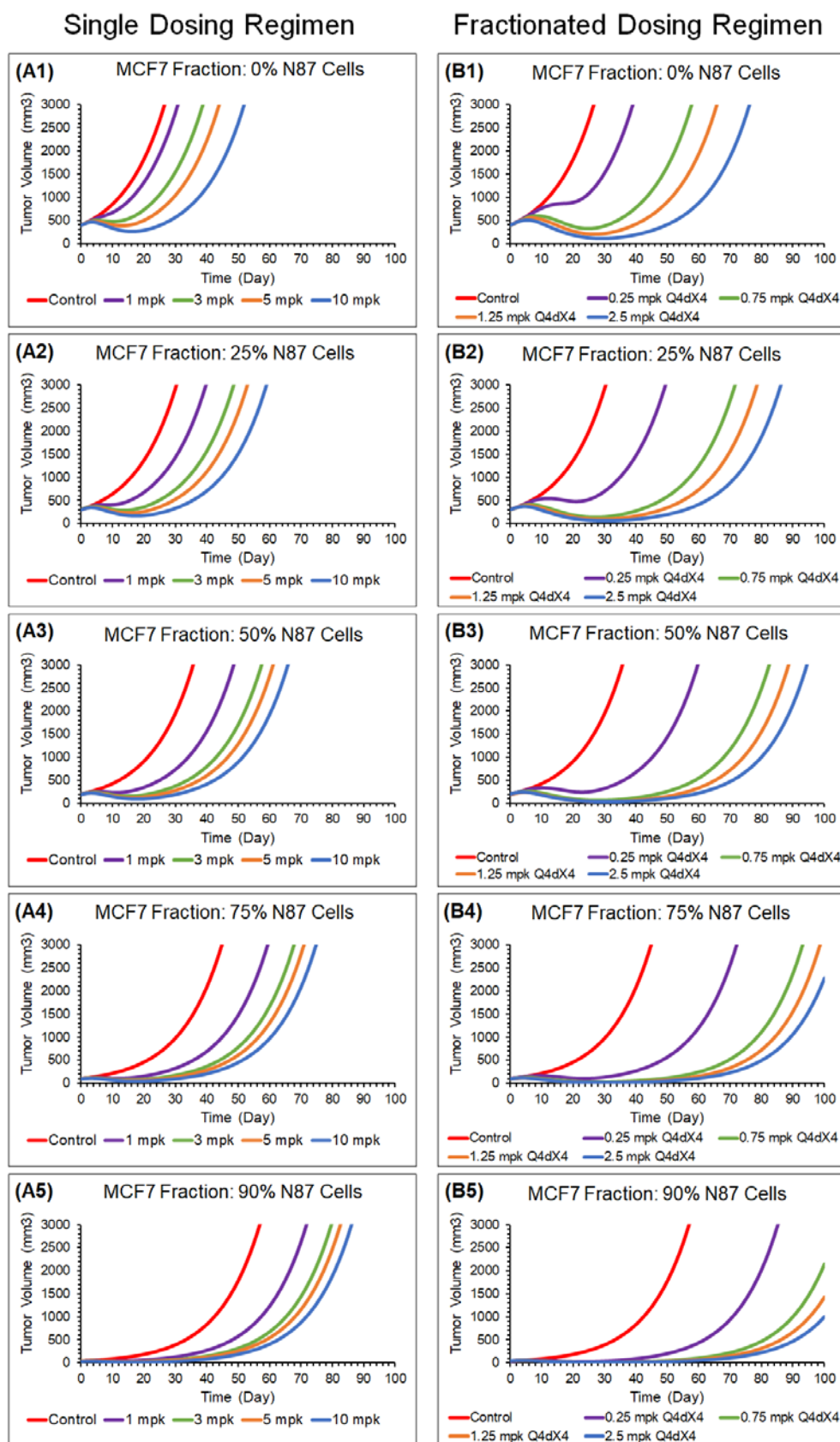


Figure 7

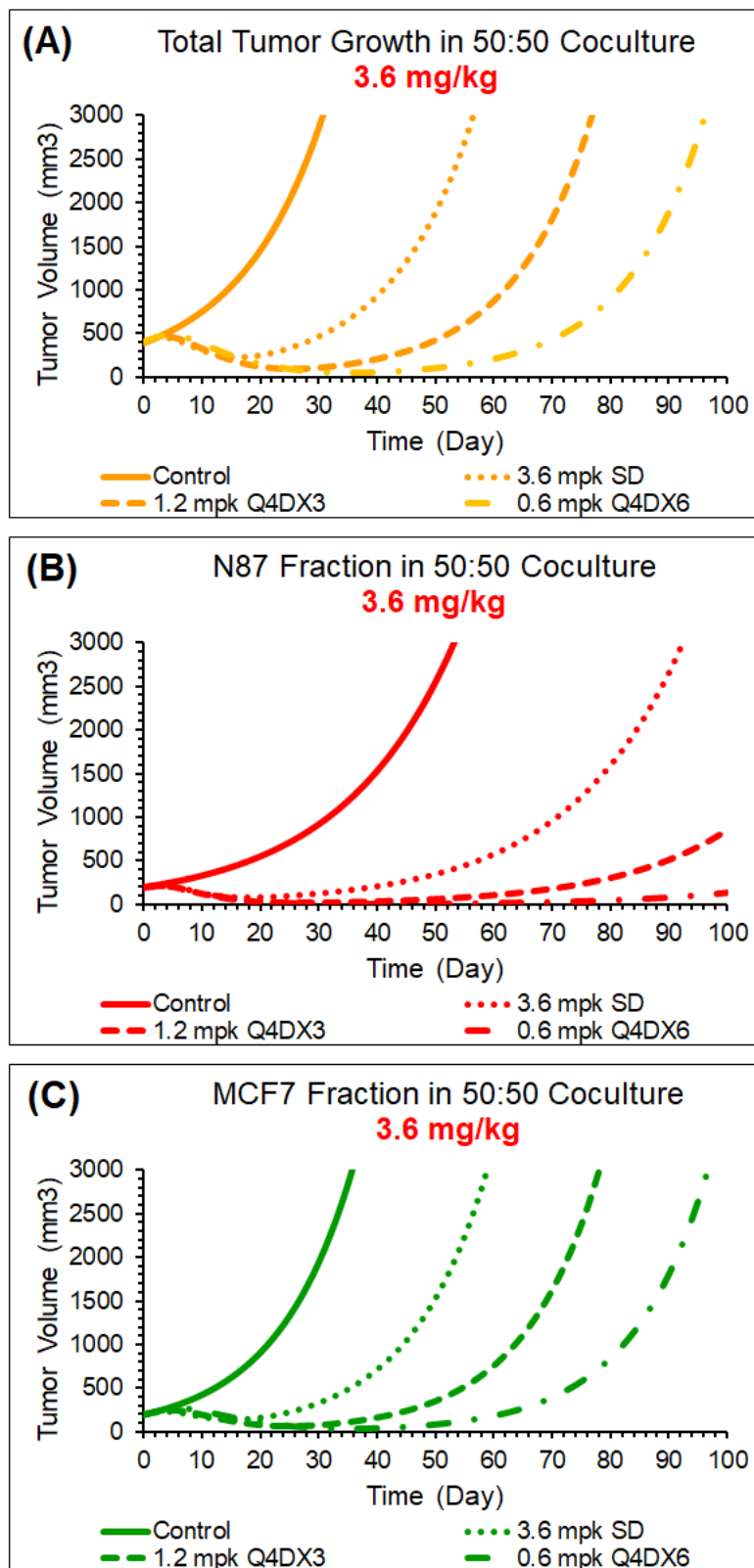


Figure 8